Mutation dynamics and fitness effects followed in single cells

Lydia Robert, Jean Ollion, Jérôme Robert, Xiaohu Song, Ivan Matic, Marina Elez

Mutation dynamics and fitness effects followed in single cells

Lydia Robert,[1,2]* Jean Ollion,[1] Jerome Robert,[1] Xiaohu Song,[3] Ivan Matic,[3] Marina Elez[1,4]*

Mutations have been investigated for more than a century but remain difficult to observe directly in single cells, which limits the characterization of their dynamics and fitness effects. By combining microfluidics, time-lapse imaging, and a fluorescent tag of the mismatch repair system in *Escherichia coli*, we visualized the emergence of mutations in single cells, revealing Poissonian dynamics. Concomitantly, we tracked the growth and life span of single cells, accumulating ~20,000 mutations genome-wide over hundreds of generations. This analysis revealed that 1% of mutations were lethal; nonlethal mutations displayed a heavy-tailed distribution of fitness effects and were dominated by quasi-neutral mutations with an average cost of 0.3%. Our approach has enabled the investigation of single-cell individuality in mutation rate, mutation fitness costs, and mutation interactions.

The pace of evolution and possible trajectories depend on the dynamics of mutation incidence and the effects of mutations on fitness. Mutation dynamics has never been analyzed directly. It is assumed to be Poissonian, but mutagenesis characterized by bursts, with transient mutation rate increases, has been demonstrated in several organisms (1–3). Muta-tion bursts may facilitate the acquisition of com-binations of mutations, which is critical to the evolution of complex traits (4). Effects of mu-tations are known to range from beneficial to deleterious or lethal, but estimating the entire distribution of fitness effects (DFE), central to evolutionary modeling, has proven challenging (5). The DFE for spontaneous mutations has been estimated with the mutation accumulation (MA) approach (*6*–*8*), whereby independent lines of individuals are propagated in conditions that minimize the effects of natural selection and the evolution of their fitness is tracked. The precision of such DFE estimations is limited because of the small number of lines that can be monitored, typically fewer than 100. In addition, only an upper boundary for the average mutational effect is obtained, or strong assumptions are made regarding the DFE shape (*9*, *10*). Finally, in MA studies of microorganisms, the mutation sample is biased, as natural selection purges lethal and strongly deleterious mutations.

We quantitatively characterized the dynamics of spontaneous point mutations arising from replication errors, a major source of mutations (*11*, *12*), and their DFE in the bacterium *Escherichia coli*. For real-time detection of mutations in single living cells, we developed a mutation visualization (MV) experiment. We also designed a microfluidic MA (μMA) experiment, which allowed us to track fitness in the complete absence of natural selection in a high-throughput fashion during the accumulation of mutations.

In μMA experiments, we grew cells in a "mother machine" microfluidic chip (*13*) (Fig. 1A) and imaged them by phase-contrast microscopy to monitor their growth and survival at the single-cell level (*14*) (Fig. 1B and movie S1). The mother machine contained a series of separate microchannels where cells grew in a single row (Fig. 1A). These microchannels were closed on one side and retained the "mother" cell abutting the dead end through consecutive divisions. Therefore, at each generation, one individual was kept independently of its fitness (Fig. 1C), thus eliminating natural selection. Malthusian fitness, the exponential growth rate at the population level, can also be defined at the single-cell level as the cell exponential elongation rate. We imaged more than 1000 microchannels in parallel, in controlled and constant conditions, every 4 min

[1]Laboratoire Jean Perrin, UMR 8237 Sorbonne Universités, UPMC Université Paris 06, Paris, France. [2]Micalis Institute, Institut National de la Recherche Agronomique, AgroParisTech, Université Paris Saclay, Jouy-en-Josas, France. [3]INSERM U1001, Université Paris-Descartes, Sorbonne Paris Cité, Faculté de Médecine Paris Descartes, Paris, France. [4]Institute of Systems and Synthetic Biology, UMR 8030, CNRS, Commissariat à l'Energie Atomique et aux Energies Alternatives, Genopole, Université d'Évry Val-d'Essonne, Université Paris Saclay, Evry, France.
***Corresponding author. Email: lydia.robert@polytechnique.org (L.R.); marina.elez3@gmail.com (M.E.)**

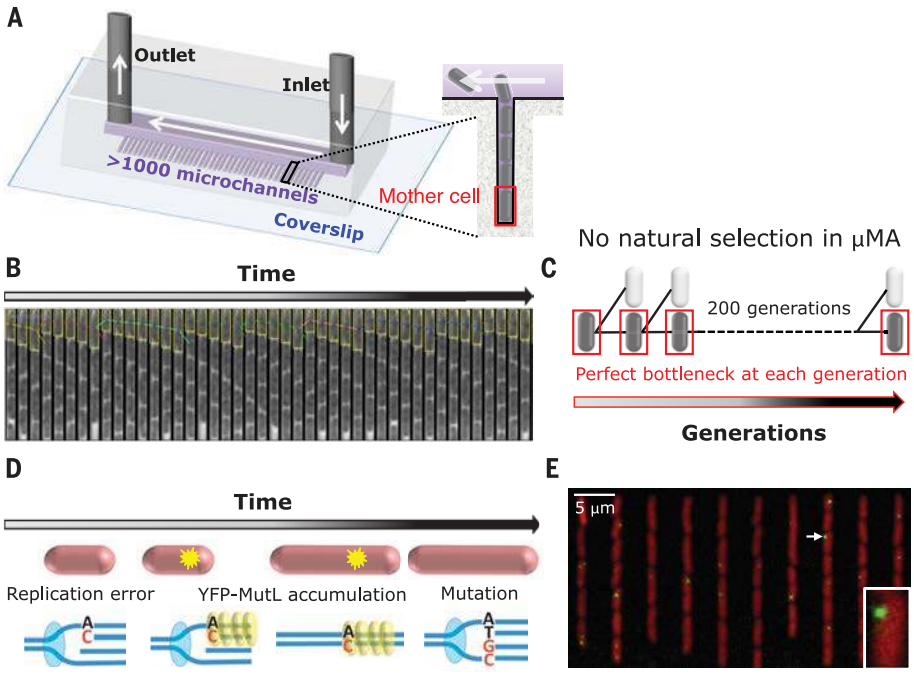

Fig. 1. Experimental setup. (**A**) The mother machine microfluidic chip, used for growing *E. coli* cells during μMA and MV experiments. μMA and MV experiments were performed independently, using phase-contrast microscopy and epifluorescence microcopy, respectively. (**B**) Phase-contrast images of one microchannel over time in a μMA experiment. We developed software that measures the mother cell length (represented by yellow boxes) at each frame and computes its fitness at each generation (*14*). (**C**) The mother machine allowed us to keep the mother cell at each division, regardless of its fitness, thus blocking natural selection. (**D**) Tracking point mutation emergence in single cells with YFP-MutL in the *mutH* strain, where all replication errors are converted into mutations. (**E**) Overlay of red (from the constitutive expression of tdCherry for automated cell segmentation) and yellow (YFP-MutL) fluorescence images from an MV experiment. The inset shows a magnified image of a cell with a YFP-MutL focus (arrow).

over the course of 3 days, which corresponded to ~200 generations. We obtained ~10^5 fitness measurements per experiment.

In MV experiments, cells grown in the mother machine were imaged by fluorescence microscopy (*14*). We visualized mutations using a fusion of yellow fluorescent protein (YFP) with MutL mismatch repair protein, which forms fluorescent foci at replication errors (*15*) (Fig. 1, D and E, and movie S2). To detect and track MutL foci, we developed an automated image analysis procedure (*14*). The dynamics of mutations originating from replication errors depends on both error production and repair. We examined the dynamics of error production by eliminating error repair through inactivation of the mismatch repair endonuclease MutH (*14*). Full inactivation was verified by control experiments (*14*). The YFP-MutL protein forms transient foci (*15*) (movie S2), and the average lifetime of the foci in the *mutH* strain corresponds to the time between the passage of two successive replication forks (*14*) (fig. S1). This pattern shows that in *mutH* cells, all MutL foci are converted into mutations by the next round of DNA replication.

Replication errors might occur at a constant rate with Poissonian dynamics, or alternatively, bursts of errors might be produced from fluctuations in intracellular composition, such as transient nucleotide pool imbalances (*1*, *3*). To investigate these possibilities, we performed MV experiments using *mutH* cells, tracking more than 3000 MutL foci in mother cells and deriving their interarrival times (the times between two successive focus occurrences) (Fig. 2A). These interarrival times were exponentially distributed and uncorrelated, which is characteristic of a Poissonian process (*14*) (Fig. 2, B and C, and fig. S2). In agreement with this finding, the number of MutL foci appearing between two frames followed a Poissonian distribution (fig. S3). As our method is limited by optical resolution, we cannot detect bursts of replication errors if they occur at a single replication fork on a short genomic region (typically less than 80 kilobases). In contrast, we can detect transient hypermutator states if they affect several replication forks, as would be expected for metabolic fluctuations, because different forks occupy different positions in the cell.

Our data indicate Poissonian dynamics rather than dynamics characterized by bursts, but they do not exclude some fluctuations in the replication error rate. In particular, we expect the error rate to depend on the number of replication forks, which changes during the cell cycle (*14*). We found a global proportionality between cell size, a proxy for the stage in the cell cycle, and the replication error rate across a range of cell sizes (fig. S4). Further analysis of the relationship between cell size and error rate revealed steplike variations reminiscent of variations in the number of replication forks (Fig. 2, D and E), with error rates varying by a factor of ~3 during a single cell cycle.

When exposed to certain external stresses, bacteria trigger specific responses that transiently increase the mutation rate (*16*–*18*). In our

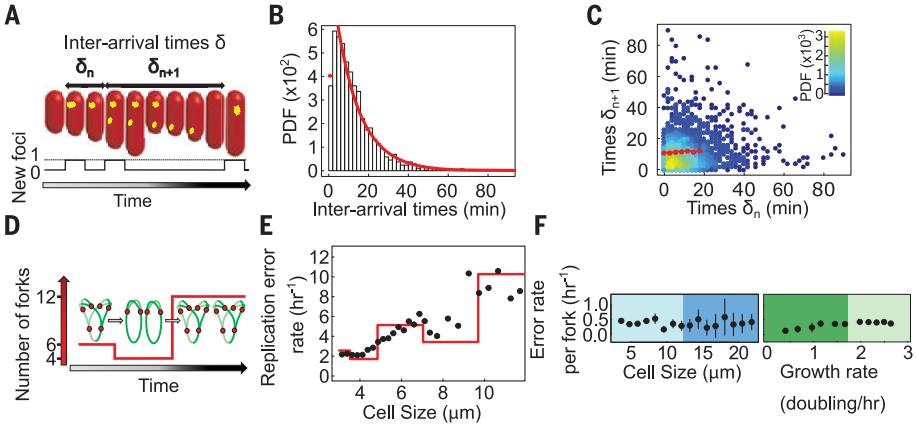

Fig. 2. Replication error dynamics. (**A**) The variables analyzed in MV experiments were the interarrival times for YFP-MutL foci (δ) and the number of new foci per mother cell. δ_n and δ_{n+1} indicate two successive interarrival times. (**B**) Histogram of focus interarrival times for a representative *mutH* experiment (n = 1873 foci). The red line and dot are predictions under the Poisson process hypothesis, which includes a correction accounting for discrete observation (*14*). PDF, probability density function. (**C**) Correlation between two successive focus interarrival times for the data in (B). Color indicates local density (inset). Red dots represent data binned according to δ_n. (**D**) Theoretical number of forks as a function of time for a doubling time of 26 min. Chromosomes are depicted in green, and the red dots denote replication forks. (**E**) Rate of replication error as a function of cell size in single cells. Black dots, experimental data; red line, prediction based on the number of forks (*14*). (**F**) Error rate per fork as a function of cell size and growth rate for single cells. Data were binned according to either cell size or growth rate. Results are means, and errors bars show ±2 SEM.

MV experiments, a small fraction of cells experienced endogenous stress, as demonstrated by reduced growth rate and/or abnormally large cell size. We investigated whether such subpopulations exhibit higher rates of replication error. To take into account the different replication fork numbers for different subpopulations, we estimated the number of forks in single cells and the mean error rate per fork in each subpopulation (*14*). Abnormally large cells and slowly growing cells did not present elevated error rates per fork (Fig. 2F and fig. S5), suggesting that stress-induced mutagenesis (SIM) acts mainly at the level of error repair or that endogenous stress in a favorable environment causes limited SIM.

Visualization of mutations and fitness measurements could in principle be combined into a single time-lapse microscopy experiment. However, simply linking one mutation to one fitness effect is impossible for two reasons: First, there can be a substantial lag between the occurrence of a mutation and its effect on fitness. Second, a MutL focus indicates the insertion of an erroneous base in one of two newly replicated DNA strands. Consequently, the progeny from a cell with a MutL focus will contain a mixture of mutant and nonmutant cells (*14*) (fig. S6). Therefore, we performed μMA and MV experiments separately, which allowed us to increase the throughput of μMA experiments.

Using MV, we estimated mutation rates for *E. coli* wild-type (WT) (~0.0022 mutation/hour) and *mutH* mutant (~0.32 mutation/hour) strains (*14*), which agree with estimations from whole-genome sequencing of MA lines of WT and mismatch repair–deficient cells (*11*). We then performed a μMA experiment with WT cells, which accumulated an average of ~0.1 mutation per mother cell line over ~60 hours. As expected, the growth rate distribution for WT cells was stable over time (Fig. 3A, left). In contrast, for *mutH* cells, which accumulated ~20 mutations per mother cell line over ~60 hours, the mean growth rate slightly decreased (Fig. 3A, middle), and some cells underwent a steplike decrease in growth rate (Fig. 3B, blue trajectory) or a total cessation of growth, indicating cell death (fig. S7). Surprisingly, the average decrease in the growth rate of *mutH* cells during μMA (~0.1% per hour) was smaller than what would be expected from previous estimates of the average effect of mutations (*7*, *19*, *20*). We also performed μMA experiments using the strain MF1 (*14*), which has a mutation rate ~20 times that of the *mutH* strain (*14*) (table S1) because of impaired proofreading (*21*). As expected, the decrease in fitness in MF1 cells was ~20 times that in *mutH* cells (Fig. 3A, right, and table S2).

We then characterized the DFE by developing a nonparametric method, with no assumptions about DFE shape (*14*). Using the probabilistic framework of MA studies, we derived all the moments of the DFE (*14*). For nonlethal mutations, our estimate of mean fitness cost (Fig. 3C) is 0.31% ± 0.04%, which is lower than previous estimates (*7*, *19*, *20*). We found that the DFE for nonlethal mutations has a coefficient of variation (CV) of 9.5 ± 1.2, a skewness of 16.6 ± 0.7, and a kurtosis of 360 ± 90 (Fig. 3C). We also

obtained moments of higher order for the DFE (table S3). These results indicate a distribution that is wide, skewed, and heavy tailed, dominated by quasi-neutral mutations relative to infrequent, strongly deleterious mutations, such as the beta distribution in Fig. 3D.

The estimated DFE for MF1 was similar to the DFE for the *mutH* strain (table S4), although these strains have different mutation spectra (*11*, *21*). To further investigate the effect of the mutation spectrum on the DFE, we performed μMA experiments using a *mutT* mutant (fig. S8), which has a mutation rate similar to that of the *mutH* strain but a specific mutation spectrum of >99% AT-to-CG transversions (*11*, *12*, *14*) (table S1). Despite the differences in the way mutagenesis occurs, we found that the DFE for the *mutT* strain did not differ substantially from the DFE for the *mutH* or the MF1 strain (table S4).

Steplike growth rate decreases such as those shown in Fig. 3B (blue trajectory) occurred during μMA in all mutator strains and not in the WT strain. They might be provoked by a single deleterious mutation, independently of previously acquired mutations, or by the accumulation of interacting mutations. To investigate this issue, we studied the rate of occurrence of growth rate decreases in *mutH* and *mutT* cells. From the analysis of all single-cell trajectories (*14*) (fig. S9), we defined two categories of cells: slow-growing cells that underwent a >30% decrease in growth rate (Fig. 4A, top) and fast-growing cells corresponding to the rest of the population. The percentage of fast-growing cells decreased exponentially over time (*14*) (Fig. 4A, bottom), demonstrating that >30% growth rate decreases are caused by single deleterious mutations with >30% fitness cost. These mutations occur at a constant rate, independently of the accumulation of previous mutations, and represent 0.3% of all mutations. As expected from the quasi-optimal growth rate of our *mutH* strain, our analysis of single-cell trajectories detected no strongly beneficial mutations (>20% effect) during μMA (*14*).

Likewise, to assess whether lethal mutations occur at a constant rate, we studied survival during μMA (*14*). The WT strain, accumulating ~0.1 mutation over the course of μMA, showed age-related mortality (Fig. 4B, left), in agreement with previous observations (*13*). The high–mutation-rate *mutH*, *mutT*, and MF1 strains exhibited additional mutation-related mortality (Fig. 4B, left). During the first ~35 hours of μMA, when the mortality rate for the WT was low and approximately constant, the survival of the *mutH*, *mutT*, and MF1 mutator strains exponentially decreased (Fig. 4B, right, and fig. S10). To further disentangle age- and mutation-related mortality, we performed a μMA experiment using the strain pMQ, which has increased proofreading deficiency compared with MF1 (*21*). pMQ cells died rapidly, and their survival decreased exponentially (Fig. 4B, right, and fig. S11). These analyses demonstrate that lethal mutations occur at a constant rate in μMA, independently of previously acquired mutations, and that ~1% of mutations are lethal.

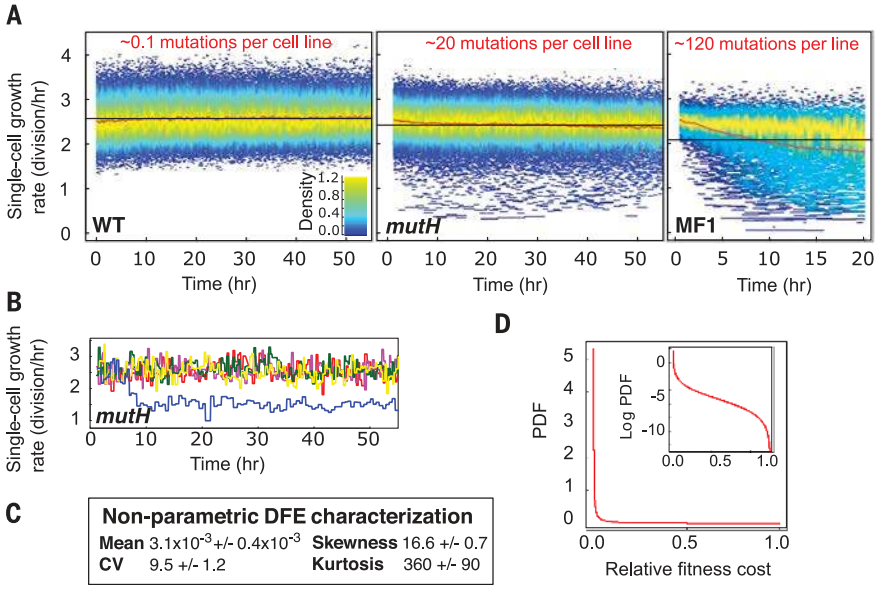

Fig. 3. μMA analysis allows nonparametric DFE characterization. (**A**) Representative μMA results for WT, *mutH*, and MF1 (*dnaQ926*) strains. For each time point, all single-cell growth rates for all mother cells are plotted (WT strain, $n = 1.8 \times 10^5$ cells; *mutH* strain, $n = 1.1 \times 10^5$ cells; MF1 strain, $n = 2.6 \times 10^4$ cells). Color depicts growth rate density. The red line represents the mean growth rate evolution. The black line indicates the mean of all growth rates. (**B**) Examples of single-cell growth rate trajectories for the *mutH* strain (one color per cell line). (**C**) Nonparametric estimation for the first four moments of the DFE allows calculation of the mean, the coefficient of variation (CV), skewness, and kurtosis (for each calculation, the mean ± 2 SEM for three independent *mutH* experiments is given). (**D**) Example of distribution with similar moments [beta distribution; parameters, $\alpha = 0.0074$ and $\beta = 2.4$, calculated to give the mean and CV as for the DFE in (C), giving skewness = 17 and kurtosis = 370]. The inset shows the same distribution on a log scale.

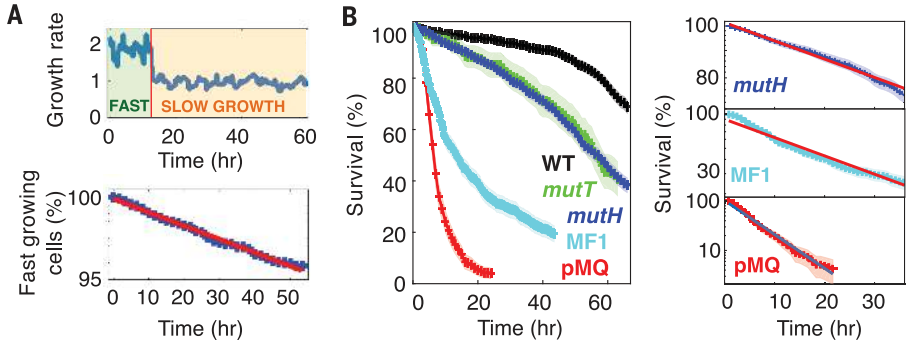

Fig. 4. Strongly deleterious (>30% cost) and lethal mutations occur at a constant rate during μMA. (**A**) The top panel shows an example of a *mutH* growth rate trajectory (blue line) corresponding to the occurrence of a strongly deleterious mutation in a mother cell. To analyze such events, we defined two categories of mother cells, slow-growing cells that underwent an abrupt, >30% growth rate decrease and fast-growing cells corresponding to the rest of the population. The bottom panel shows the temporal evolution of the percentage of fast-growing cells (represented by blue dots, on a log scale; we analyzed 5272 single-cell trajectories and found 156 strongly deleterious mutations). The 95% confidence interval is narrower than the line thickness. The red curve is an exponential fit (coefficient of determination $R^2 = 0.99$). (**B**) The left panel shows survival curves of the population for the WT ($n = 1283$ single-cell trajectories), *mutH* ($n = 1480$), *mutT* ($n = 216$), MF1 ($n = 838$), and pMQ ($n = 472$) strains. The 95% confidence intervals are represented by the shaded areas (they are narrower than the line thickness for $n > 400$). The right panel shows the same survival curves on a log scale for *mutH* (data in blue, exponential fit in red; $R^2 = 0.99$), MF1 (data in cyan, exponential fit in red; $R^2 = 0.99$), and pMQ (data in red, exponential fit in blue; $R^2 = 0.99$) strains. The plot is limited to ~35 hours, during which age-related mortality was low and approximately constant. The 95% confidence intervals are represented by the shaded areas.

Our results show that the accumulation of mutations with <30% fitness cost does not change the rate of lethal or strongly deleterious mutations (>30% cost), as would be expected from the saturation or induction of a buffering mechanism (*22*, *23*). We anticipate that examination of various suboptimal genotypes in μMA experiments would allow further investigation of mutation interactions and provide a complete picture of epistasis, central to the evolution of sexual reproduction and recombination (*24*). Our approach may also allow for investigation of how the DFE and mutation dynamics change in response to the environment, shedding light on the adaptation potential of populations.

REFERENCES AND NOTES

1. J. W. Drake, *Crit. Rev. Biochem. Mol. Biol.* **42**, 247–258 (2007).
2. S. Uphoff *et al*., *Science* **351**, 1094–1097 (2016).
3. J. Wang *et al*., *Proc. Natl. Acad. Sci. U.S.A.* **104**, 8403–8408 (2007).
4. M. R. Stratton, P. J. Campbell, P. A. Futreal, *Nature* **458**, 719–724 (2009).
5. T. Bataillon, S. F. Bailey, *Ann. N.Y. Acad. Sci.* **1320**, 76–92 (2014).
6. T. Mukai, *Genetics* **50**, 1–19 (1964).
7. T. T. Kibota, M. Lynch, *Nature* **381**, 694–696 (1996).
8. P. D. Keightley, A. Caballero, *Proc. Natl. Acad. Sci. U.S.A.* **94**, 3823–3827 (1997).
9. A. Eyre-Walker, P. D. Keightley, *Nat. Rev. Genet.* **8**, 610–618 (2007).
10. D. L. Halligan, P. D. Keightley, *Annu. Rev. Ecol. Evol. Syst.* **40**, 151–172 (2009).
11. H. Lee, E. Popodi, H. Tang, P. L. Foster, *Proc. Natl. Acad. Sci. U.S.A.* **109**, E2774–E2783 (2012).
12. P. L. Foster, H. Lee, E. Popodi, J. P. Townes, H. Tang, *Proc. Natl. Acad. Sci. U.S.A.* **112**, E5990–E5999 (2015).
13. P. Wang *et al*., *Curr. Biol.* **20**, 1099–1103 (2010).
14. Materials and methods and supplementary text are available as supplementary materials.
15. M. Elez *et al*., *Curr. Biol.* **20**, 1432–1437 (2010).
16. R. S. Galhardo, P. J. Hastings, S. M. Rosenberg, *Crit. Rev. Biochem. Mol. Biol.* **42**, 399–435 (2007).
17. P. L. Foster, *Crit. Rev. Biochem. Mol. Biol.* **42**, 373–397 (2007).
18. R. Maharjan, T. Ferenci, *Mol. Biol. Evol.* **32**, 380–391 (2015).
19. S. Trindade, L. Perfeito, I. Gordo, *Philos. Trans. R. Soc. London Ser. B* **365**, 1177–1186 (2010).
20. L. Perfeito, A. Sousa, T. Bataillon, I. Gordo, *Evolution* **68**, 150–162 (2014).
21. K. M. Esvelt, J. C. Carlson, D. R. Liu, *Nature* **472**, 499–503 (2011).
22. S. Maisnier-Patin *et al*., *Nat. Genet.* **37**, 1376–1379 (2005).
23. T. A. Sangster, S. Lindquist, C. Queitsch, *Bioessays* **26**, 348–362 (2004).
24. R. D. Kouyos, O. K. Silander, S. Bonhoeffer, *Trends Ecol. Evol.* **22**, 308–315 (2007).

ACKNOWLEDGMENTS

We thank M. F. Bredeche, S. Fleurier, L. Becerra, and M. Rosticher for technical assistance; O. Tenaillon, A. Amir, N. Henry, P. Thomen, G. Debregeas, A. F. Bitbol, V. Vargas, R. Robert, D. Chatenay, and M. De Paepe for discussions and comments on the manuscript; and N. Kuperwasser for manuscript editing. **Funding:** This study was funded by the Agence Nationale de Recherche (grant ANR-14-CE09-0015-01). **Author contributions:** M.E. and L.R. designed research and performed experiments. L.R., J.O., and M.E. analyzed the data. M.E. and L.R. wrote the manuscript with input from all authors. L.R. performed modeling. J.O. developed image analysis software. J.R., I.M., and X.S. contributed tools. **Competing interests:** The authors declare no competing interests. **Data and materials availability:** The data described in the paper have been archived at Dryad (doi:10.5061/dryad.75625), and software codes and programs are available at Github (https://github.com/LabJeanPerrin/BOA).

Supplementary Materials for

Mutation dynamics and fitness effects followed in single cells

Lydia Robert,* Jean Ollion, Jerome Robert, Xiaohu Song, Ivan Matic, Marina Elez*

1 Materials and Methods

1.1 Microfabrication and microfluidics

In the chip that we used for this study, the microchannels are $\sim$25μm long and $\sim$1 μm wide and high (height between 0.95 and 1.1 μm and width between 1 and 1.5 μm) and they are regularly spaced with a 4 μm period. The main trench is 15mm long, 50 μm wide and $\sim$30 μm high.

We fabricated several master molds by laser lithography. Two steps of lithography are necessary to get different heights for the microchannels and the main trench. For aligning the mold between the two steps, Aluminium (AL3X35N Neyco) marks were first deposited on a silicon wafer (wafers4p Neyco) by metal evaporation. To improve the adhesion of photoresist to the wafer, a thin layer of Microchem's Omnicoat was deposited by spin-coating 35s at 3000rpm with acceleration 300 rpm/s, and baked 1 minute on a hotplate at 200°C. Then SU-8 2002 was spin coated at 1000 rpm for 30s and baked 1 minute on a

hotplate at 95°C. The microchannels were then patterned by laser lithography (UV laser writer DWL 66FS Heidelberg) and the photoresist was baked 2min on a hotplate at 95°C, developed 10s in Microchem's SU-8 developer and baked at 150°C for 5 min. Microchannels height was checked with a mechanical profilometer (Dektak 150 Veeco). For patterning the main trench, SU-8 2015 was spin-coated for 30S at 2000rpm, baked 4 min on a hotplate at 95°C, patterned with the laser and baked 6 min on a hotplate at 95°C, developed 2 min in Microchem's SU-8 developer and baked 5 min on a hotplate at 150°C. The height of the main trench was measured with a profilometer.

To fabricate the chips from the molds we used standard soft lithography techniques. We used RTV-615 PDMS from Momentive, with A/B ratio of 10:1. PDMS was poured on the mold, degassed under vacuum and cured overnight at 65°C. Holes were drilled in the chip using a WPI Biopsy punch of 0.75mm diameter. The PDMS was sealed to a glass cover slip using a 30s oxygen plasma treatment (Harrick Plasma). To improve the bonding, the chip was incubated 10 minutes at 100°C after sealing. To prevent bacteria from sticking to the glass slide, we then incubated the chip with 10 mg/ml Bovine Serum Albumin for 2 hrs at room temperature. To load the bacteria into the microchannels, an overnight culture was concentrated 10-20 times by centrifugation and injected into the chip. Cells can swim inside the microchannels spontaneously but with varying efficiency. Cells were usually incubated 1hr in the chip at room temperature and if channel loading was insufficient the chip was sometimes centrifuged several minutes at 300rpm (the chip was orientated such that the centrifugal force pushes the cells inside the microchannels on one side of the chip). To deliver the growth medium into the chip during the experiment, we used a Harvard Apparatus PHD Ultra syringe pump set at 2ml/hr, Monoject 140 ml syringes with LS23 needles (Phymep), Tygon S54-HL flexible tubing (Phymep) and steel couplers SC23/8 (Phymep).

1.2 Microscopy

For fluorescence imaging we used an inverted Delta Vision Elite microscope equipped with the Ultimate Focus system for automatic focalization, a 100x oil immersion objective (N.A. 1.4), a temperature-controlled chamber, and the DV Elite sCMOS Camera. Fluorescence illumination was provided by the DV Light Solid State Illuminator 7 Colors at 575 nm (mCherry excitation) and 513 nm (YFP excitation). During time-lapse experiments images were taken every 2 minutes ($\sim$10 images per cell cycle) for 24 hrs, using 0.1s exposure with illumination intensity set at 3.5% of the maximum LED intensity for mCherry, and 2s exposure at 7.5% of the maximum LED intensity for YFP. During the cell cycle,YFP-MutL foci can move in the z direction inside the cell, potentially creating variations of intensity between frames and perturbing image analysis. To limit such variations we used a special imaging mode for YFP images, called Optical axis integration, which allows collecting and integrating one continuous image through an extended Z movement. Each YFP image is therefore a 2D Z projection of the 1μm interval around the cell focal plane.

For μMA experiments we used an inverted Nikon Eclipse Ti-E microscope equipped with the Perfect Focus system for automatic focalization and an external phase contrast unit, a Plan APO 100x oil immersion objective (N.A. 1.4), a temperature-controlled chamber,

and a Uniblitz VMM-D1 shutter. Illumination was provided by a 100W halogen lamp and images were taken with 50ms exposure. Images were acquired using the Hamamatsu CCD C8484-05G Camera. During time-lapse experiments, images were taken every 4 minutes (∼5 images per cell cycle) during ∼70h (∼200 cell cycles). We performed all experiments at 37°C.

1.3 Image analysis

We developed a high-throughput image analysis software for the analysis of bacteria growing in the "mother machine", based on several java-based libraries ([25, 26, 27]).

1.3.1 Fluorescence Experiments:

Bacteria are visible in the Red fluorescence channel (RFP) and foci in the Yellow fluorescence channel (YFP)

Pre-processing of RFP and YFP images

First, for each YFP or RFP image, background fluorescence is removed. Background pixels are first automatically determined in the whole image using the Kappa Sigma Clipping algorithm [28]. Then the background is removed line by line in each image by subtracting for each line the mean background pixel value. The RFP fluorescence of single-cells exhibits some heterogeneity, with rare cells reaching a fluorescence that is 5- to 20-fold higher than the average value, potentially perturbing further image processing. To solve this problem we developed an algorithm that automatically saturates the histogram of image containing such cells, based on the difference between the Otsu threshold [29] and the Kappa Sigma Clipping [28] threshold. In order to set the micro-channels along the y-axis, with the dead-end at the top, both YFP and RFP images are automatically rotated by an algorithm based on the radon transform. Next, we correct the XY drift over time using the Lucas-Kanade algorithm, with a reference frame that changes every 20 frames to avoid error accumulation.

Detection of micro-channels

In fluorescence, the PDMS structures are not visible. Therefore the channels are detected using the RFP fluorescence expressed by the bacteria growing inside the channels, by a simple thresholding using Kappa Sigma Clipping algorithm [28]. The segmentation of channels is done at each frame, then the detected objects are tracked over time, then the dimensions of each micro-channel is normalized over frames.

Detection of bacteria within the channels

First, high frequency noise is removed using a median filter and low frequency signal is removed by subtracting a large-scale Gaussian transform. The image is then thresholded using

a constant threshold, creating a mask containing the bacteria. At this stage, several bacteria can be fused and considered as a single object (under-segmentation). To separate the bacteria, a watershed algorithm is applied to the maximal eigenvalue of the Hessian transform within the mask. This step generates over-segmentation, that is reduced by merging adjacent regions according to a criterion based on the Hessian transform value normalized by the Gaussian transform value, at the boundaries of the regions.

Tracking of bacteria

We developed a tracking algorithm that allows local correction of segmentation errors using information at previous and next frames. In the dead-end micro-channels, the rank of the cells within one channel is directly linked to their position in the lineage, the old pole mother cell being at the closed end of the channel. Tracking is done according to this rank. In order to detect division events as well as segmentation errors, we introduced minimum and maximum thresholds for the ratio of sizes between two frames (0.85 to 1.5). When this ratio is below the minimum threshold, we consider that a division occurred. When segmented objects with very different sizes are present, several assignment solutions are possible within the same window of size ratio. To compare them, we defined an assignment score based on the median size ratio at 10 previous frames, allowing to take into account variations in growth rate. When the size ratio exceeds the maximum threshold, it can either be due to over-segmentation at previous frame(s), or under-segmentation at the current (and next) frame(s). The two correction scenarios are compared using two different criteria, a cost function based on the Hessian transform, as introduced in the segmentation step and the number of corrected tracking errors. The best scenario is applied, if it allows to correct tracking has a cost under a pre-defined threshold.

Detection of foci

In order to attenuate the effect of cell-to-cell variability in YFP fluorescence background, the distribution of pixel values inside each cell is normalized by subtracting its mean and dividing by its standard deviation. In addition, we do not work directly with fluorescent levels but on a Laplacian-of-Gaussian (LoG) transform of the image, which is more robust to fluctuations in foci and background fluorescence intensity. More precisely, foci are detected using a seeded watershed algorithm on the LoG transform. Seeds are determined as regional maxima in the LoG image, and filtered using a threshold on a quality parameter defined as the square root of the product of the LoG value and Gaussian value.

Tracking of foci

We use the TrackMate [30] implementation of the Jaqaman [27] algorithm, allowing efficient tracking of several foci and including a procedure for gap-closing. In order to take into account cell growth, the coordinates of detected foci used for distance calculation is expressed relatively to the nearest cell pole or cell center. In order to reduce false positives, detected foci are divided into two categories, low quality and high quality, according to the quality

parameter defined previously. Low quality spots are included in the tracking step only if they can be linked to a high quality spot. To achieve this, low and high quality are first linked all together, then tracks containing only low quality spots are removed, then tracking is performed once again, this time only with remaining objects.

1.3.2 Phase Contrast Experiments

Pre-processing

The image is first rotated as described in the section "Pre-processing of RFP and YFP images", then background is subtracted using ImageJs' subtract background.

Detection of microchannels

Phase contrast fringe is automatically detected based on an intensity criterion and image is cropped. Micro-channel end is detected as the extrema in the Y-derivative image averaged in the X-direction. To detect horizontal bounds: the image X-derivative is averaged in the Y-direction and bounds are detected as extrema separated by a gap corresponding to the micro-channel width. The segmentation is done at each frame, then the detected objects are tracked over frames, then the dimensions of each micro-channel is normalized for all frames.

Detection of Bacteria

First images are thresholded using a threshold based Otsu's method [29]. For robustness purpose, the threshold is computed using a sliding widow over frames. This step can lead to under-segmentation. Regions are then split using a watershed algorithm on the euclidean distance map, which produces over-segmented regions. Regions are then re-merged using a criterion on the 1D-curvature of the contour of the segmented objects.

Tracking of Bacteria

The tracking method is identical in the analysis of phase contrast and fluorescence images, except that the cost function for correction scenario is based on the 1D-curvature of the contour of segmented object, as defined in the segmentation step.

1.4 Mutant frequency measurement in batch cultures

We estimated the genome-wide mutation rate of WT and *mutH* with the MutL foci method ($\mu_{WT,foci}$ and $\mu_{mutH,foci}$). In addition, for all our strains we performed classical genetic assays that allow determining the frequency of mutants resistant to rifampicin or streptomycin arising during growth of bacterial population in batch cultures (table S1).

For these assays we grew strains overnight in LB, except the strain with the inducible dominant negative mutant of the polymerase proofreading subunit dnaQ926, which was grown in Glucose Minimal Medium.The overnight cultures were diluted 10^6-fold in LB or Minimal Medium supplemented by 1% arabinose for inducible dnaQ926 expression, grown

to saturation and plated on selective medium (LB agar containing 100 μg/ml rifampicin or LB containing 100μg/ml streptomycin) to select rifampicin resistant (RifR) colonies or streptomycin resistant colonies (StrepR) and on LB agar to determine the total number of colony forming units. Colonies were scored after 24h of incubation at 37°C. The average mutant frequency was determined for each strain from three to six independent experiments.

We estimated the ratio of the mutation rate of each strain to the mutation rate of *mutH*(r_{MF1}, r_{mutT} ...), simply by dividing the frequency of Rif (or Strep) mutants obtained with a given strain by the frequency of Rif (or Strep) mutants obtained for *mutH* (e.g.r_{mutT}=$freq_{mutT}/freq_{MutH}$). Then for each strain S we estimated the genome-wide mutation rate as being this ratio r_S multiplied by $\mu_{mutH,foci}$. We therefore obtain an estimation of the mutation rate for *mutT* (0.37/hr) and *MF1* (5.6/hr). The estimated mutation rate of *mutT* is therefore similar to *mutH* mutation rate. Consistently, measurements using whole-genome sequencing were previously performed by Lee et al and Foster et al. ([11] [12]) and showed that the mutation rate in *mutT* strain is the same as the mutation rate in a MMR deficient strain (0.149 mutations per generation for *mutT* and 0.151 for *mutL*).

1.5 Analysis of fitness data from μMA to estimate the moments of the DFE

Using our image analysis software (1.3), we extracted the data on cell sizes from the phase contrast images. Single cells elongate exponentially between birth and division, while their width stays constant. Single-cell growth rate (i.e. fitness) is therefore defined as the rate of cell elongation. For each microchannel we used only the data from the cell abutting the dead-end, the so-called mother cell.

The segmentation errors generated by image analysis can create aberrant, very low or high growth rates. Therefore, we filtered our data in the following way. For each channel and each generation, we calculated the median of the growth rates for earlier generations (M_{before}) and subsequent generations (M_{after}). Growth rate estimates that are clearly aberrant (as confirmed by visual inspection of images) are either much larger than both M_{before} and M_{after} or much smaller than both M_{before} and M_{after} (Note that M_{before} and M_{after} can be significantly different because of the occurrence of deleterious mutations). Therefore for each generation, we remove the value of the growth rate μ from the data if it differs from both M_{after} and M_{before} by more than a threshold value T ([$\mu - M_{before} > T$ and $\mu - M_{after} > T$] OR [$\mu - M_{before} < -T$ and $\mu - M_{after} < -T$]). The value T was fixed at 30% of the average growth rate in the experiment, corresponding to the mean+/−2*standard deviation of the variable $\mu - M_{after}$ (or equivalently $\mu - M_{before}$; both variables follow a distribution that is well approximated by a gaussian). The datasets for all strains (WT *mutH*, *mutT*, and MF1 such as plotted in Figure 3A and Figure S8) were all filtered using the same procedure. In order to eliminate any image analysis errors that could bias our results and would not have been removed by this filtering procedure, we selected all the channels where a growth rate smaller than 0.015 was detected and systematically checked by visual inspection cell segmentation and tracking on all the images corresponding to this channel. Therefore, small growth rate values are all valid measurements.

Death of slowly growing cells induces noise in DFE estimation (figure S14). Therefore, to estimate the DFE's first moments (figure 3C and table S3) we used a subset of the data, restricted in time and containing only cells that do not die on this restricted time window (time points before 40 hours, only channels where the mother cell is still alive at 44 hours). For selecting such data we use an automatic procedure. If the growth rate of a cell is below 0.003 (10% of its initial value) during more than 80 minutes, the cell and its potential descendants are removed from the data. We checked that the results obtained through this automatic procedure are identical to those obtained when removing dead cells detected by visual inspection of the phase contrast images, as shown in table S8 for a representative *mutH* experiment.

We estimated the slopes of $E_1(t)$, $E_2(t)$, ... $E_{10}(t)$, for all the μMA experiments with WT, *mutH*, *mutT* and MF1 strains (see table S3). The slope of $E_n(t)$ is the product of the mutation rate λ with the n^{th} moment of the DFE (see section 2.3.2). For *mutH*, the mutation rate λ is determined from our MV experiments ($\lambda = 0.32\ hr^{-1}$; see section 2.2.3).The mutation rate for *mutT* and MF1 is estimated using classical genetic assays (section 1.4), giving 5.6/hr for MF1 and 0.37/hr for *mutT*.

In order to compare the DFE to a Beta distribution we estimated the two shape parameters α and β of the Beta distribution from the estimated mean m and variance v of the DFE. $\alpha = m^2(1-m)/v - m \sim 0.0074$ and $\beta = (1-m)/m(m^2(1-m)/v - m) \sim 2.4$.

1.6 Detection of strongly deleterious mutations

For detecting strongly deleterious mutations, we detected abrupt decreases of growth rate in mother cells by computing at each generation the median of the growth rates for earlier generations (M_{before}) and subsequent generations (M_{after}). This was done after data was filtered to remove aberrant growth rate values (see section "Estimation of the moments of the DFE from experimental data", subsection "Data analysis"). When the growth rate is stable, the difference $\Delta = M_{before} - M_{after}$ is small. In contrast, when there is an abrupt decrease of growth rate, as depicted in figure 4A, Δ has a higher, positive value. We defined abrupt decreases of growth rate by using a threshold value for Δ equal to 30% of the average growth rate, which is high enough to allow reliable detection by this procedure. In addition we systematically checked the segmentation and tracking of all the images for the channel where a decrease of growth rate was detected.

For determining more precisely the timing of occurence of the growth rate decrease, we used a different quantity δ_t, defined as the difference between the average growth rate of the six generations before and the average growth rate of the six generations after. δ_t allows a precise timing of the event because it shows a sharp peak when the growth rate decreases (see figure S9). Because of mortality, the number of cells decreases substantially between the beginning and the end of the experiment (in the *mutH* strain, typically 2/3 of the mother cells are dead at the end of the experiments). Therefore, the time series of growth rates (W_t in section 2.3.1) can have very different lengths for different channels, introducing an important data censoring effect. To take this into account in our study of deleterious mutations occurence (as shown in figure 4A), we performed an analysis as

described in section 1.9 for survival. The instantaneous rate of strongly deleterious mutations is calculated as the number of cells acquiring such a mutation during a time interval divided by the number of cells "at risk", i.e. still alive at the beginning of the time interval. The bottom panel of figure 4A is a reconstruction using these rates (therefore correcting for the decreasing number of cells during the experiment). Confidence intervals are calculated with the formula mentioned in section 1.9 for survival analysis (see [31]).

1.7 Strains

For the experiment on the mutation accumulation dynamics, we used the MG1655 strain 63ME121R, constructed for this study. It expresses *yfp-mutL* from the Plac promoter and *tdCherry* from the PRNA1 promoter on the chromosome. It is inactivated for the native *mutL* and *mutH* genes. *yfp-mutL* expression allows real-time mutation detection, where mutations are detected as bright spots of YFP-MutL [15]. *tdCherry* expression allows cell segmentation during image analysis. *mutL* deletion prevents the obstruction of mutation visualization by the non fluorescent version of MutL while *mutH* inactivation results in all replication errors being converted to mutations. We constructed the strain 63ME121R in four steps. First, we inactivated the *mutL* gene of the wild-type sequenced MG1655 strain obtained from *E. coli* Genetic Stock Center (CGSC 6300) by replacing the wild-type *mutL* allele with the *mutL::kan* allele using P1 transduction. This resulted in the strain MG1655mutL. Second, we replaced the *lacZ* gene of MG1655mutL by the *yfp-mutL-cat* construct from the strain ME120 using P1 transduction. We described the ME120 strain previously in [32]. This resulted in the strain 63ME120. Third, we integrated into the strain 63ME120, between two Tn7 insertion sites, the PRNA1 promoter-*tdCherry* sequence. This was done by transforming into 63ME120, the pNDL-32 temperature-sensitive, ampicillin-resistant plasmid obtained from Johan Paulsson's lab (http:/openwetware.org/wiki/Paulsson:Strains). Upon transformation, we selected on LB agar plates supplemented with 100μg/mL ampicillin, then streaked twice at 30°C and once at 42°C on LB agar to get rid of the plasmid. We confirmed the plasmid loss by checking that selected clones were red and ampicillin-sensitive. This resulted in the strain 63ME120R1. The CatR and KanR cassettes were then removed from 63ME120R1 by site-specific recombination between FRT sites, using the pCP20 plasmid, as described by Wanner et al. [33], producing the strain 63ME120R. Finally, we inactivated the *mutH* gene of the 63ME120R strain by replacing the wild-type *mutH* allele with the *mutH::cat* allele using P1 transduction. This resulted in the strain 63ME121R.

For inducible expression of *dnaQ926* mutant from PBad promoter on the chromosome we integrated the *araC*-PBad-*dnaQ926* DNA into prophage P21 attachement site using the Clonetegration method [34]. This was done in five steps. First, we PCR-amplificied the *araC*-PBad-*dnaQ926* fragment from the plasmid pMQ [21]. Second, we cloned *araC*-PBad-*dnaQ926* fragment into kanamycin resistant pOSIP-KT plasmide containing attP21 and P21 integrase[34]. This resulted in pOSIP-KTdnaQ926. Third, we transformed pOSIP-KTdnaQ926 into MG1655 by selecting on kanamycin. Fourth, we checked by PCR that pOSIP-KTdnaQ926 integrated into attP21 site on the MG1655 chromosome. This resulted in strain MF0. Fifth, to remove from the chromosomal attP21 site the pOSIP-KTdnaQ926

integration module including the antibiotic marker (KanR) we transformed MF0 with temperature sensitive pE-FLT plasmid expressing the FLR recombinase [34] and selected on ampicilin at 30°C. We checked for the excision of the antibiotic marker and neighbouring sequences by PCR and we got rid of the plasmid pE-FLT by growing MF0 ON at 37°C. This resulted in the strain MF1.

For all other experiments we used the wild-type *E. coli* MG1655 (CGSG 6300) strain and its derivatives listed in table S9, generated by P1 transduction and transformation. We verified the strain genotypes by testing for different phenotypes such as the capacity to generate mutations conferring resistance to rifampicin or expression of the fluorescent protein.

1.8 Media

We grew cells in LB medium at 37°C. During growth in microchannels, LB medium was supplemented with 100μg/ml Bovine Serum Albumin (BSA) to prevent cell adhesion in the main channel. For mutation visualization we added 1mM IPTG to induce *yfp-mutL* expression. For μMA experiments with the inducible dominant negative mutant of the polymerase proofreading subunit dnaQ926 (strains pMQ and MF1), cells were grown overnight in Glucose minimal medium (M9, 2mM MgSO4, glucose 0.4%) to repress dnaQ926 expression (supplemented for pMQ with Streptomycin 10 μg/ml and Spectinomycin 100 μg/ml to prevent plasmid loss). After cells were loaded into the chip, a first flow of LB+BSA+glucose 0.4% (+Streptomycin 10 μg/ml +Spectinomycin 100 μg/ml for pMQ) was applied during 1 hr, to re-initiate cell growth without induction of dnaQ926. Then the medium was switched to LB+BSA+arabinose 1% (+Streptomycin 10 μg/ml for pMQ) to induce dnaQ926 expression and time-lapse experiment started 1 hr after to ensure full induction.

1.9 Survival analysis

After death, the cell's aspect can change, in particular its morphology and intensity in phase contrast. This can result in segmentation and tracking errors in automatic image analysis that limit the precision with wich cell death can be automatically detected. To estimate the mortality rates (figure 4B), we therefore detected the death of cells abutting the channels dead end by visual inspection of phase contrast images. We define cell death as an abrupt cessation of growth and division (fig S7). Also, during the experiment, some cells can escape the channels, by swimming away. Such incomplete observation events, so-called censored data, can bias the survival curve and the estimation of the death rate if not properly taken into account. Altought they are rare in our experiments (typically less than 10% of the channels) we took them into account by performing an appropriate, classical survival analysis, as described in [35]. The principle of this analysis is to calculate an instantaneous death rate (q_t) as the number of cells that die in a given time interval (d_t) divided by the number of cells that were "at risk" at the beginning of the interval (i.e. that were alive and had not escaped, $n_{atrisk,t}$): $q_t = d_t/n_{atrisk,t}$. Survival curves such as presented in figure 4B are then reconstructed using these instantaneous death rates : denoting S_t the percent of

survivors (as plotted in figure 4B), $S_t = 100 \prod_{i=0}^{t-1}(1 - q_i)$. These survival curves therefore correspond to a fictive cohort. Approximate 95% confidence intervals are calculated as in [35], using the formula in Peto et al. [31] : The 95% confidence interval is $[S_t - 1.96 \times SE_t, S_t + 1.96 \times SE_t]$, with $SE_t = S_t \sqrt{\frac{(1-S_t/100)}{n_{atrisk,t}}}$

2 Supplementary Text

2.1 Validation of fluorescent MutL foci method for mutation visualization

2.1.1 Foci quantification with our software is robust to variations in detection parameters

As explained in section 1.3, regional maxima in the LoG image are considered as true foci only if their quality parameter is above a certain threshold. In addition, the detected foci are then divided into two categories corresponding to different levels of confidence ("high quality" and "low quality" foci), based on another threshold on the quality parameter. The values for these two thresholds have been tested in order to yield the best results (as assessed by visual inspection). Importantly, we checked that our foci detection procedure is robust to changes in these parameters. We chose a reasonable range for each threshold (such that outside this range the segmentation was clearly aberrant), and we measured the mutation rate for several combinations of parameter values within these ranges. We found only 8% variation in the estimated mutation rate, i.e. the coefficient of variation of the distribution of estimated mutation rate is 8%. This low variation demonstrates that our method is robust to parameter changes and allows a precise quantification of MutL foci.

2.1.2 Mutation rate estimation using MutL foci in *mutH* are in excellent agreement with previous estimates from the literature

From MV experiments with *mutH* strain, we estimated the MutL foci rate from the number of new foci occurrence per frame or from the mean foci inter-arrival time (these two estimates are coherent, showing less than 10% difference). From the rate of MutL foci, we estimated the mutation rate as explained in section 5.3. Our mutation rate estimate is 0.32 mutations/hr. In order to compare with previous literature we can convert this rate per time unit in a rate per generation, simply by multiplying it by the population doubling time (here 26 minutes). We find 0.14 mutations/generations, which is in excellent agreement with the recent estimate of mutation rate in a MMR-deficient *mutL* strain, determined by Mutation Accumulation and Whole Genome Sequencing ([11]; 0.15 mutations/generation). This strongly supports the fact that MutL foci in *mutH* correspond to unrepaired errors that are converted to mutations.

2.1.3 The lifetime of MutL foci in *mutH* confirms that all tagged mismatches are converted into mutations

We checked that each MutL focus is converted to a mutation in *mutH* by testing the prediction that the foci lifetime should equal the arrival time of the next replication fork. Note that the inter-arrival time of replication forks is equal to the doubling time [36]. We found that the foci lifetime distribution resembles a gaussian, with a mean very close to the doubling time (see figure S1; for this experiment mean focus lifetime is $\sim$ 23min and mean doubling time is $\sim$ 25 min). This indicates that the focus generated by a replication fork stays at the replication error until the next fork comes and converts the error into a mutation This strongly indicates that as expected in a *mutH* strain, replication errors are not repaired and MutL foci tags nascent mutation.

2.1.4 No false-positive, mismatch-independent MutL foci

We quantified the rate of false positive, i.e. replication error-independent MutL foci, by performing MV experiment using a double mutant *mutH mutS*. We found that the rate of false positives is very low, potentially accounting for only 0.08% of MutL foci in *mutH* strain.

2.1.5 *mutH* inactivation results in all replication errors being converted to mutations

Very similar mutation rate in MMR- *mutH* strain (our data) and MMR- *mutL* strain ([11]) suggests that MutH is as responsible as MutL for repair of replication errors, in agreement with previous genetic studies [37]. In order to confirm this in our conditions we inactivated *uvrD*, the helicase acting downstream of MutH, and performed MV experiment using the *uvrD* strain. The rate of MutL foci in *uvrD* is similar to the rate in *mutH* (0.31 mutations/hr vs 0.32 mutations/hr) and importantly, foci lifetimes are also similar in *uvrD* and *mutH* (mean 24 min vs 23 min). This result indicates that MutH is essential to mismatch repair. Likewise, we found very similar MutL foci rate and foci lifetime distributions in *mutH rnhB* and *mutH* (0.25 vs 0.32 mutations/hr, and mean foci lifetime of 22min vs 23 min), suggesting that unlike in *B. subtilis* or in eukaryotes [38], Ribonucleotide Excision Repair (RER) RnhB ribonuclease can not substitute for MutH during MMR.

2.1.6 MutL foci can be used to follow mutations in MMR proficient cells

Contrarily to *mutH*, where the repair of errors by MMR is inactivated, in wild type (WT) cells with proficient MMR repair, two kinds of foci are distinguishable: very short-lived foci with lifetime < 4 min, accounting for 98% of all foci (total number of foci analyzed :1572), and 2% of long-lived foci, with lifetime similar to *mutH* foci. Short-lived foci may correspond to repaired errors. In agreement with this hypothesis, MMR is known to repair $\sim$ 99% of mismatches [39]. Nevertheless, demonstrating that short-lived foci are indeed

repaired replication errors requires further investigation. In contrast, the lifetime of long-lived foci (similar to the lifetime of *mutH* foci) strongly suggests they are unrepaired errors that will be converted into mutations. In agreement with this interpretation, the number of long-lived foci in WT is $\sim$ 130 x lower than the number of foci in a *mutH* background, which has a 100-200x higher mutation rate (in particular MMR deficient strain has a rate $\sim$ 150 x higher than WT according to whole genome sequencing of MA lines [11]). From the rate of occurrence of long-lived foci we can estimate the rate of mutation in WT, as explained in section 2.2.3, and we find 0.0022 mutations/hr. Simply by multiplying this value by the population doubling time (here $\sim$ 0.43 hr), we find a rate per generation of $\sim 10^{-3}$ mutations/generations, in excellent agreement with previously reported estimations of mutation rate in WT *E. coli* (in particular Lee et al. reported 0.87 10^{-3} and 1.14 10^{-3} for whole genome sequencing of two MA experiments [11]). In addition, this number of long-lived foci is increased in a mutant expressing a mutant allele of the polymerase proof-reading subunit, of a factor consistent with its elevated mutation rate. All this constitutes strong evidence that long-lived foci correspond to unrepaired replication errors that are converted to mutations. Our method therefore also allows reliable estimation of the mutation rate of MMR proficient strains.

2.1.7 Biological contexts limiting mutation visualization using MutL foci

We found that the number of MutL foci in *mutT* is $\sim$ 60 times lower than in *mutH*, whereas the mutation rate of the two strains are similar. This discrepancy is expected since the incorporation of oxidatively-damaged nucleotides is poorly recognized by MMR [40]. This shows that MutL foci cannot be used to detect mutations arising from incorporation of oxidatively-damaged nucleotides. Mutations originating from other chemically-altered bases may be also poorly detected by MutL foci. Importantly, MMR can be subject to down-regulation in some stressful conditions [41, 42] or can become limiting in some conditions [43, 44]. In such conditions our method is not appropriate to detect mutations.

2.2 Data analysis of fluorescent foci dynamics

2.2.1 Discrete observation of a poisson process at regular time intervals deforms the exponential distribution of inter-arrival times

To test if mutations follow a poisson process we determined the distribution of foci inter-arrival times, i.e. time intervals between two successive foci. In a Poisson process, the inter-arrival times are exponentially distributed. Nevertheless, the observation of a Poisson process at discrete, regular times (time interval δ) introduces a bias in the estimated distribution. If the observed inter-arrival time is 0, the real inter-arrival time is in $[0,\delta[$. In contrast, observed inter-arrival times of $n\delta$ $(n > 0)$ correspond to events occuring with a real time delay in $](n-1)\delta, (n+1)\delta[$, an interval twice larger than for $n = 0$. This leads to a deformation of the exponential distribution, with an under-representation of very small inter-arrival times. We can derive an analytical formula for such distribution as follows. Let us consider the inter-arrival time X between fluorescent foci following an exponential law of parameter λ.

The first observation of the first focus will occur a time delay U after its appearance. The times of observation being independent of the mutations process, U is a random variable following a uniform distribution between 0 and δ (δ : time between consecutive images). Therefore the observed inter-arrival time T is given by : $T = \delta\,(\lfloor \frac{X-U}{\delta} \rfloor + 1)\,\mathbb{1}_{X>U}$. From this, we find that the law of observed inter-arrival times is :

$$P(T = 0) = 1 - \frac{(1 - e^{-\lambda\delta})}{\lambda\delta} \tag{2.1}$$

$$P(T = n\delta) = \frac{e^{-(n-1)\lambda\delta}}{\lambda\delta}(1 - e^{-\lambda\delta})^2 \quad \text{, for } n > 0 \tag{2.2}$$

To validate this formula we performed simulations of a Poisson process observed at regular time intervals. We show in figure S2 that the distribution of simulated inter-arrival times indeed follows the law defined by equations 2.1 and 2.2.

2.2.2 Estimation of the number of replication forks in single cells

We estimate the number of replication forks in a single cell depending on its rate of growth and cell cycle stage. This estimation is based on common knowledge of the bacterial cell cycle ([36], [45]), such as explained in [36], where a nice program of Cell Cycle Simulation (CCSim) is presented [36]. Our model is similar to the one in [36], the required parameters are the C and D periods, which are respectively the constant time required to replicate the chromosome (C period) and the constant time between replication termination and division (D period), and a cell size parameter (i.e. the average size of bacterial cells growing at a given rate). We use classical values for C and D periods, i.e. respectively 40min and 20 min and the cell size parameter is fitted such that the average cell size we measure corresponds to the average rate of growth we measure. Using only these parameters we can estimate the number of forks of any single cell from its size and its rate of growth. We can then estimate the mean error rate per fork in a cell population, such as in Figure 2F, by normalizing the number of MutL foci occurrences in a single cell at a given time step by its predicted number of forks.

2.2.3 Estimation of the mutation rate from the rate of MutL foci occurrence, taking into account multifork replication and DNA segregation

The distribution of observed inter-arrival times between two fluorescent foci follows an exponential distribution of parameter Λ, corrected for discrete observation as explained in section 2.2.1. The mean inter-arrival time is therefore $\frac{1}{\Lambda}$. This allows estimating Λ, the rate of fluorescence focus occurrence. For the *mutH* strain in LB medium we find $\Lambda = 2.7$ hr^{-1} and $\Lambda = 2.6$ hr^{-1} in two independent experiments. Because a focus tags a replication error that will give rise to a mutation and not the mutation itself, the rate of foci occurrence cannot be directly interpreted as the rate of mutation. We estimated the mutation rate from the replication error rate based on the following considerations. The passage of the

replication fork generates two double-stranded DNA molecules, therefore four DNA strands. If a replication error occurs, one strand carries a mutated base, whereas the three other strands carry the parental base. Therefore 1/4 of the strands at this fork are mutated (figure S6A). Consequently, in conditions where DNA replication cycles do not overlap, 1/4 of the descendants of the cell where the error occurs will be mutants (figure S6B). An additional complexity comes from the fact that at fast growth, the cell undergoes multifork replication, i.e. several cycles of DNA replication overlap, and all replication forks are not equivalent. When a given fork incorporates an erroneous base at a given locus, the proportion of mutants in the cell's descendants depends on the number of copies of that locus inside the cell. As an example, if 6 forks are present in the cell (see figure S6C and D), corresponding to two overlapping replication cycles, two of them (red dots in figure S6) replicate loci that have not already been replicated and are present as a single copy, leading to a proportion of mutants in the progeny of 1/4 (figure S6C). In contrast, the 4 other forks (yellow dots in figure S6) replicate loci that are already present in two copies inside the cell, on the two partly replicated chromosomes, leading to a mutated base in one of the 8 strands of this locus in the cell, i.e. 1/8 of mutants in the cell's progeny (figure S6D). Therefore, in this example a replication error can lead to a proportion of mutants in the descendants of 1/4 or 1/8, depending on which fork generates the error. Taking all this into account, we can calculate the proportion p of mutant cells in the descendants of a cell where a fluorescent focus appears. The mutation rate when only one cell is kept at each generation, as in our μMA experiment will therefore be given by the product Λp. In our Mutation Visualization experiments, the doubling time is around 26 minutes. Therefore the cell has in average 7 replication forks : 6 forks between age 0 min and 6min, 4 forks between age 6 min and age 18 min, and 12 forks between age 18 min and 26 min (see section 2.2.2 and [36]). The case with 6 replication forks is shown in figure S6C and D. The case with 4 replication forks is as shown in fig S6B but with two chromosomes. Likewise, the case with 12 forks corresponds to two chromosomes with 6 forks such as shown in figure S6C and D. We can therefore calculate that in our MV experiments, $p = 0.12$.

In conclusion, in our conditions the rate of mutation λ in a *mutH* strain is $\lambda = 0.12\Lambda = 0.32$ hr^{-1}. Note that this also corresponds to the rate of replication errors in a MMR-proficient strain.

As explained in the main text (p.6), in our MV experiments where fluorescent foci are followed, a small subpopulation of cells exhibits a lower rate of growth and therefore has a lower number of replication forks and a lower mutation rate (see figure S15). In order to investigate quantitatively whether this subpopulation of cells has a substantial impact on our mutation rate estimation we performed the following numerical simulations. We measured the growth rate of each single cell in the population of cells of a typical *mutH* MV experiment. We estimated the average number of replication forks corresponding to each growth rate, using common knowledge of the bacterial cell cycle (see section 2.2.2). The number of replication forks is a good estimation of replication error rate, as shown in the main text (p.6). We then simulated inter-arrival times for the heterogeneous cell population using exponential laws with parameters corresponding to the estimated single-cell replication

error rates. From the distribution of inter-arrival times that we obtained we estimated the replication error rate of the population, as done for the experimental data. We found that the estimated mutation rate is only 2% below the rate of the "normally" growing cells. Therefore the small subpopulation of slowly growing cells has a very low impact ($< 2\%$) on the estimation of the global mutation rate.

2.3 Non-parametric characterization of the DFE in μMA

In this section we first describe a probabilistic framework that is classical in MA studies and allows modeling fitness evolution during mutation accumulation (2.3.1). Then we derive analytical formula for all the moments of the DFE in this framework (2.3.2) and extend the classical model to the single-cell level (2.3.4). Finally, we investigate quantitatively the effect of mutation rate decrease through time during μMA (due to slowing down of growth during mutation accumulation) on our estimation of DFE moments (2.3.5).

2.3.1 Probabilistic model of fitness evolution during mutation accumulation

We used a simple mathematical description of the mutation accumulation process. We consider a series of mutations occuring according to a Poisson process of intensity λ ($\mathcal{P}(\lambda t)$), with relative effects s_i on fitness (W_t):

$$s_i = \frac{W_{t_{i-1}} - W_{t_i}}{W_{t_{i-1}}}, \quad i > 0$$

W_t : fitness at time t; s_i : relative effect of mutation number i

Hence, assuming that mutations have independent effects, s_i are independent, identically distributed variables and :

$$\frac{W_t}{W_0} = \prod_{i=1}^{N_t}(1 - s_i), \qquad N_t \sim \mathcal{P}(\lambda t) \tag{2.3}$$

Therefore, the model is based solely on two assumptions, the poissonian occurence of mutations, which is validated by the results of our Mutation Visualization (MV) experiments as shown in Figure 2, and the independent effects of mutations, which is validated by our results on fitness evolution in μMA experiments. Our results indeed show that accumulation of mild-effects mutations does not lead to any significant acceleration or deceleration of fitness reduction (see figure S16) and that strongly deleterious and lethal mutations occur at a constant rate (Figure 4), independently of the accumulated mild-effects mutations.

2.3.2 Calculating the moments of the DFE from the moments of the fitness distribution

Using the mathematical model introduced in section 2.3.1 (Equation 2.3), we can calculate the moments of all orders of W_t from the moments of the DFE. We will assume $W_0 = 1$

without loss of generality. $\mathbb{E}()$ stands for mathematical expectation. The k^{th} moment of W_t is :

$$\begin{aligned}\mathbb{E}(W_t^k) &= \mathbb{E}(\mathbb{E}(\prod_{i=1}^{N_t}(1-s_i)^k|N_t)), \quad k>0\\ &= \mathbb{E}(\mathbb{E}((1-s)^k)^{N_t})\\ &= \sum_{i=1}^{\infty} e^{-\lambda t}\frac{\lambda^i t^i \mathbb{E}[(1-s)^k]^i}{i!}\\ &= e^{-\lambda t}e^{\lambda t \mathbb{E}[(1-s)^k]}\end{aligned}$$

We define $E_n(t) = \sum_{k=1}^{n}(-1)^k\binom{n}{k}\ln(\mathbb{E}(W_t^k))$. We can calculate $E_n(t)$ as follows:

$$\begin{aligned}E_n(t) &= \sum_{k=1}^{n}(-1)^k\binom{n}{k}[-\lambda t + \lambda t\mathbb{E}[(1-s)^k]]\\ &= \lambda t\sum_{k=1}^{n}(-1)^k\binom{n}{k}\sum_{l=1}^{k}(-1)^l\binom{k}{l}\mathbb{E}(s^l)\\ &= \lambda t\sum_{l=1}^{n}\mathbb{E}(s^l)\sum_{k=l}^{n}(-1)^{k-l}\binom{k}{l}\binom{n}{k}\end{aligned}$$

We have

$$\binom{k}{l}\binom{n}{k} = \frac{n!}{l!(n-k)!(k-l)!} = \binom{n-l}{k-l}\binom{n}{l}$$

Thus,

$$\begin{aligned}E_n(t) =& \lambda t\sum_{l=1}^{n}\mathbb{E}(s^l)\binom{n}{l}\sum_{k=l}^{n}(-1)^{k-l}\binom{n-l}{k-l}\\ &= \lambda t\sum_{l=1}^{n}\mathbb{E}(s^l)\binom{n}{l}(1-1)^{n-l}\\ &= \lambda t\mathbb{E}(s^n)\end{aligned}$$

In our μMA experiments, W_t is measured in a thousand independent cell lines, allowing calculating $\mathbb{E}(W_t^k)$ for any $k>0$. Therefore, in order to estimate the moment of order n of the DFE ($\mathbb{E}(s^n)$), we plot $E_n(t) = \sum_{k=1}^{n}(-1)^k\binom{n}{k}\ln(\mathbb{E}(W_t^k))$ as a function of time t and estimate the slope, which is $\lambda\mathbb{E}(s^n)$, as illustrated in Figure S16. It is worth noting that we make no assumptions on the deleterious or beneficial nature of mutations and our procedure estimates the moments of the DFE of all mutations.

2.3.3 Data filtering during analysis of μMA does not bias the estimation of the moments of the DFE

As explained in section 1.5, we applied a filtering procedure to clean the data from aberrant growth rate values. This filtering and the exact value of the threshold parameter T has little impact on the quantification of the moments of the DFE, as shown in table S5 and S6.

We limited the noise induced by mortality by using a subset of the data containing only cells that do not die on a restricted time window (see section 1.5). Although less precise, an analysis on the whole data leads to similar conclusions. Table S7 shows the result of this analysis, performed on the data containing all time points and all channels (for cells dying in the course of the experiment, 10 generations before death were removed to avoid a potential decrease of growth rate linked to cell death). This analysis also shows a heavy-tailed, very skewed and leptokurtic distribution, although the quantification is less precise.

2.3.4 Extending the model to the single-cell level shows that measurement noise and phenotypic variability do not affect our estimation of the DFE's moments

In our experiments, growth rate is measured at the single cell level. In addition to the fitness of the cell's genotype at time t W_t, our measure G_t is affected by the measurement noise and a potential phenotypic variability of growth. We show in this section, by including in our model a noise term accounting for phenotypic variability and mesurement noise, that these two components do not affect estimation of the DFE moments with our method. As the single-cell growth rates measured in a clonal population (corresponding to variations of G_t when W_t is constant) are normally distributed with limited inheritance from mother to daughter ([13] and Figure S17 A and B), we introduce a white noise ϵ_t in the model (i.e. the derivative of the Brownian motion). This noise could be introduced in a multiplicative ($G_t = W_t(1+\epsilon_t)$) or in an additive way ($G_t = W_t + \epsilon_t$). If the mean single-cell growth rate changes, for instance due to a mutation or a change of environment, a multiplicative noise leads to a proportionnal change in the standard deviation of measured growth rates (a change in W_t leads to a proportional change in G_t). In contrast, in the case of an additive noise, a change of the mean of single-cell growth rate does not affect the growth rate standard deviation (standard deviation of G_t does not change when W_t changes). It has been shown experimentally that single-cell growth rate has higher standard deviation in a rich environment, compared to a poor medium [46], suggesting a multiplicative noise. To confirm that this holds as well in our experiments, we calculate the mean and the standard deviation of growth rates for cells that grow slowly due to strongly deleterious mutations. More precisely, for each channel where a strongly deleterious mutation occur, we can compute the growth rates for all the generations after the mutation and estimate the mean and standard deviation of these growth rates.

The analysis shows that the standard deviation and the mean are correlated (figure S17 C). We therefore use in our model a multiplicative noise.

We define G_t as the measured fitness (measured single-cell growth rate), while W_t is the

real underlying fitness of the cell's genotype.

$$G_t = W_t(1+\epsilon_t) \quad \text{with } \epsilon_t \text{ a white noise independent of } W_t$$

We can calculate the moments of G_t as a function of the moments of W_t and ϵ_t. By independence of ϵ_t and W_t :

$$ln(\mathbb{E}(G_t^k)) = ln(\mathbb{E}(W_t^k)) + ln(\mathbb{E}[(1+\epsilon_t)^k])$$

ϵ_t is stationary so the right-hand term does not depend on time t. Therefore the slope of $ln(E(G_t^k))$ is the same as the slope of $ln(E(W_t^k))$. The noise does not affect our estimation of the moments of the DFE.

Note that our estimation method is also robust to the introduction of a phenotypic lag τ (time delay between the occurrence of a mutation and its effect on fitness). In this case Equation 1.1 is changed for

$$\frac{W_{t+\tau}}{W_0} = \prod_{i=1}^{N_t}(1-s_i), \qquad N_t \sim \mathcal{P}(\lambda t) \tag{2.4}$$

Following the calculations in section 1.2, it is easy to show that in this case $E_n(t) = \lambda(t-\tau)\mathbb{E}(s^n)$. Consequently, the phenotypic lag does not change the slope of $E_n(t)$ and our estimation of the DFE moments.

2.3.5 Impact of mutation rate decrease during μMA on DFE characterization

During μMA experiments, cells accumulate mutations and their growth rate changes. In our conditions, mutations are mostly deleterious and the average growth rate decreases through time. At the single-cell level, the replication error rate depends on the rate of growth, through the number of replication forks present in the cell (see figure S15). Therefore, the mutation rate should decrease during our μMA experiments, which is not taken into account by the model developped in section 2.3.1. We therefore investigated quantitatively, through numerical simulations, in which conditions this effect could significantly bias our estimation of DFE moments.

We performed numerical simulations of μMA experiments according to the two following scenarios:

A. First we simulated a thousand independent cell lines accumulating mutations according to a simple Poisson process (with a single, constant rate). The effect of each mutation on growth rate is randomly drawn from a Beta distribution with parameters alpha=0.0074 and beta=2.4 (i.e. the parameters that give the same mean and variance as the DFE that we estimated experimentally, see figure 3). We added a gaussian noise to the single-cell growth rate, as observed in the data (see section 2.3.4).

B. Then we performed the same kind of simulations but instead of a constant mutation rate we used a mutation rate that depends on growth rate, through the number of replication

forks (see section 2.2.2 and figure S15). Therefore a deleterious mutation decreases both the growth rate and the mutation rate of the cell.

We first used the mutation rate estimated for our *mutH* strain. Figure S18 shows a representative example of simulations of scenario A (constant mutation rate), which resemble the experimental results of *mutH* and *mutT*. We performed 30 simulations of scenario A and 30 simulations of scenario B and found that the evolution of the growth rate distribution was very similar for the two scenarios and the difference between estimated moments was very small (see table S10).

Then we used a 20 times higher mutation rate, corresponding to our MF1 strain (with a chromosomic dnaQ926 allele). We found that for this higher mutation rate a significant difference appears between the moments estimated from simulations with scenario A or B (see table S11). Nevertheless, if moments of the DFE are estimated only on the beginning of the experiment where the fraction of slowly growing cells is still limited, the difference between scenario A and B vanishes. In particular, as shown in table S12, for this mutation rate, taking only the 10 first hours of the experiment reduces the bias in DFE moments estimation to a reasonable extent, the difference between scenario A and B being of the same order of magnitude as the variability between replicate experiments.

2.4 Mortality in pMQ strain is due to mutations

In the pMQ strain, the dnaQ926 allele is located on a streptomycin-resistant plasmid. Therefore we checked that death is not due to plasmid loss in the growth medium containing streptomycin. We therefore compared the mortality with or without induction of dnaQ926. Although there is some residual dnaQ926 expression in the absence of inducer (arabinose), the death rate was more than 30 times lower (fig S11). Therefore, mortality induced by plasmid loss is negligible compared to mutation-induced mortality.

Figure S 1: **Distribution of MutL foci lifetime for a representative** *mutH* **MV experiment** In this experiment the mean cell doubling time is 25 min

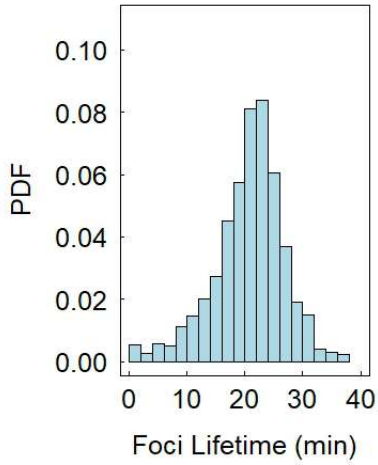

Figure S 2: **Inter-arrival time distribution of a Poisson process with discrete observation**
Probability Density Function of inter-arrival times for simulated data (red dots; we simulated a Poisson process of intensity 0.1 and in order to simulate the effect of discrete observation with time interval $\delta = 1$ we approximated the times of arrival T_i by $\lfloor T_i \rfloor + 1$; the inter-arrival times are calculated as $T_{i+1} - T_i$, for $i > 0$). Our analytical derivation of the probability law (equations 2.1 and 2.2) is represented with blue triangles.

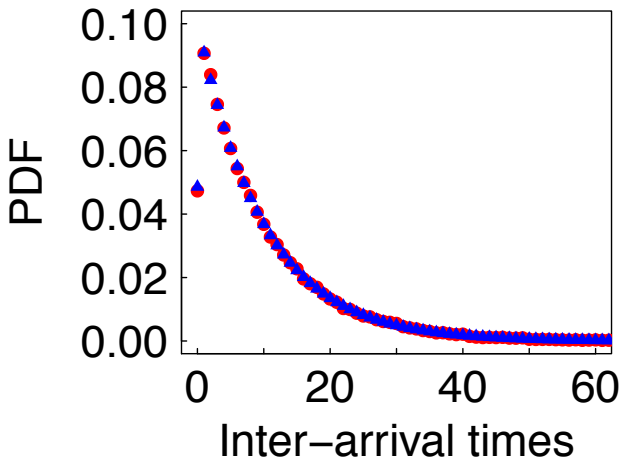

Figure S 3: **The number of foci occuring between two frames is Poisson-distributed.** Histogram of the number of new foci occuring during the two minutes time interval between two frames (light blue, log-scale, n=11275) and a Poisson distribution (red dots) with a parameter λ estimated from panel Fig. 2B. PDF: Probability Density Function.

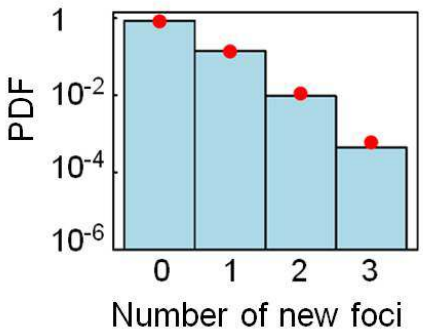

Figure S 4: **The replication error rate is proportionnal to the cell size**.
Black dots represent experimental data, binned by cell size (i.e. rates of foci occurrence are averaged for subpopulations of cells with similar size) and the red line is a linear regression with a null intercept (i.e. the slope is the only fitting parameter). The bin size here is much larger than for figure 2F. Such large bin size smoothes the step-like variations that can be observed in figure 2F and emphasizes the global proportionnality between error rate and cell size.

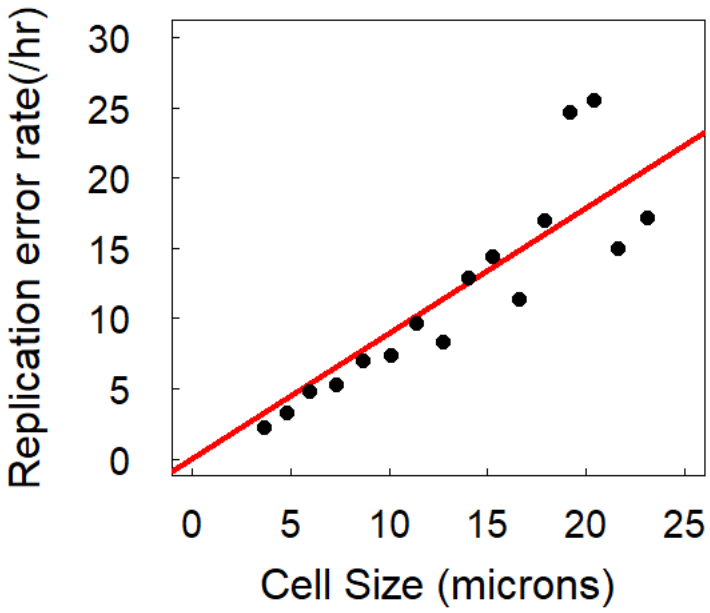

Figure S 5: **Slow-growing and long cells do not present elevated rates of replication errors per fork** Mean error rate per fork for subpopulations of cells with particular size or growth rate (see Fig.2F; error bars are Mean +/- 2 SEM). Left : mean error rate for cells with length smaller (light blue) or longer (dark blue) than 12 μm; right: mean error rate for cells with growth rate smaller (dark green) or larger (light green) than 1.7 doublings/hrs. NS: no significant difference according to t-test (p-value =0.2) ; * significant according to t-test (p-value 0.0005).

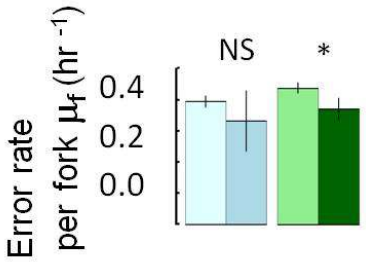

Figure S 6: **Occurrence of replication error and proportion of mutants in the progeny**

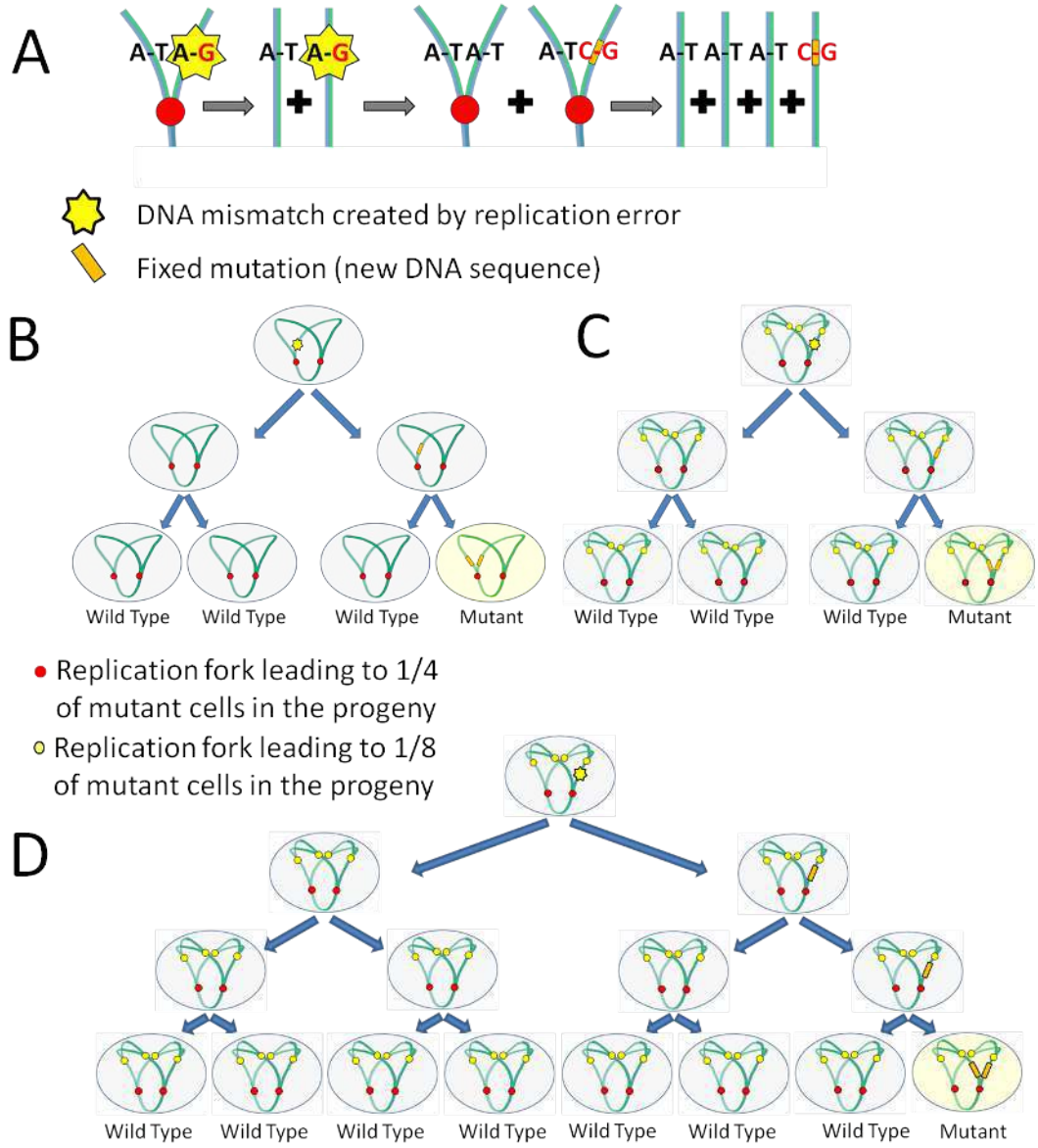

Figure S 7: **Representative example of cell death** Temporal montage of phase contrast images of a single channel where a mother cell dies; result of automatic image analysis are also shown in the bottom panel.

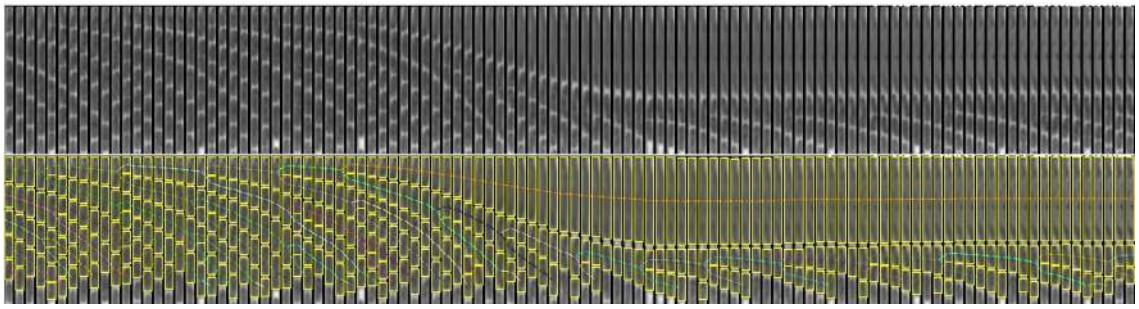

Figure S 8: **Temporal evolution of the single cell growth rate distribution in μMA experiment with a *mutT* strain.**
For each time point, all growth rates are plotted. Color depicts the local growth rate density (from blue to yellow). The red line is the evolution of the mean growth rate.

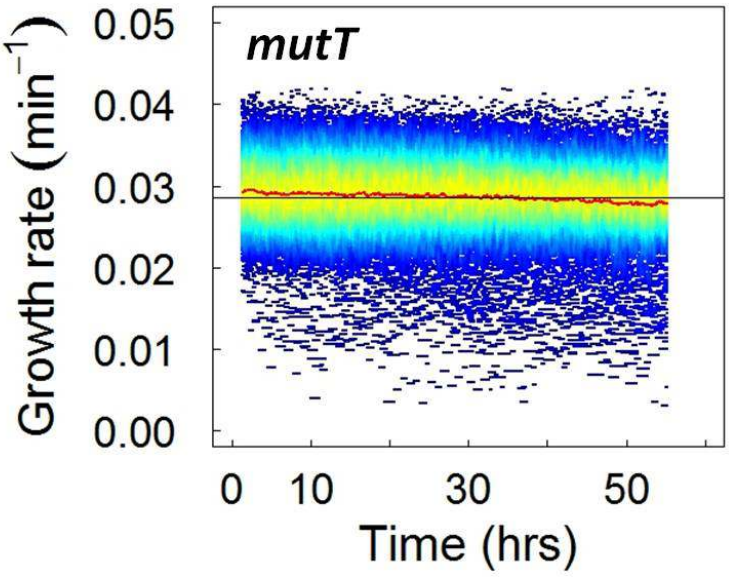

Figure S 9: **Automatic detection of abrupt decreases of growth rate** Growth rate trajectory for a microchannel where a strongly deleterious mutation occur (top panel) and evolution of δ as a function of time (bottom panel; δ is the difference between the average growth rate of the six generations before and the average growth rate of the six generations after); δ presents a sharp peak when the growth rate suddenly decreases; the maximum value of delta gives the timing of the growth rate decrease, as shown with the vertical red line.

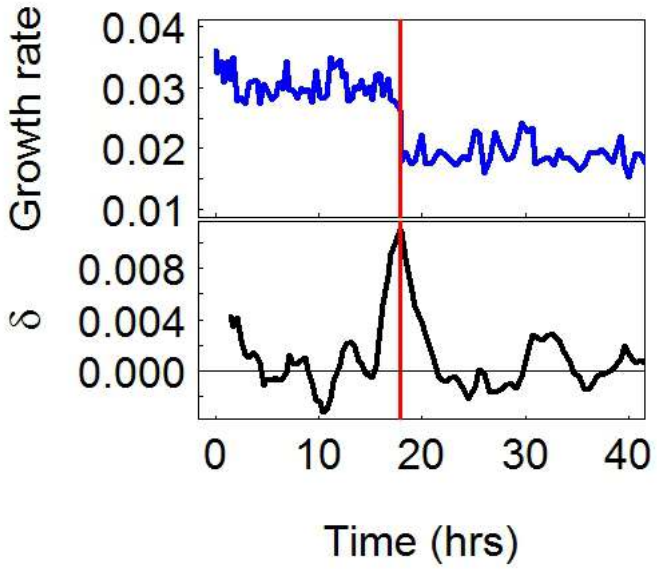

Figure S 10: **Survival of the *mutT* strain in a μMA experiment.** Survival is plotted in log-scale. In blue : survival analysis of experimental data (95% confidence interval is plotted in thin blue lines); in red: exponential fit (a line here in log scale)

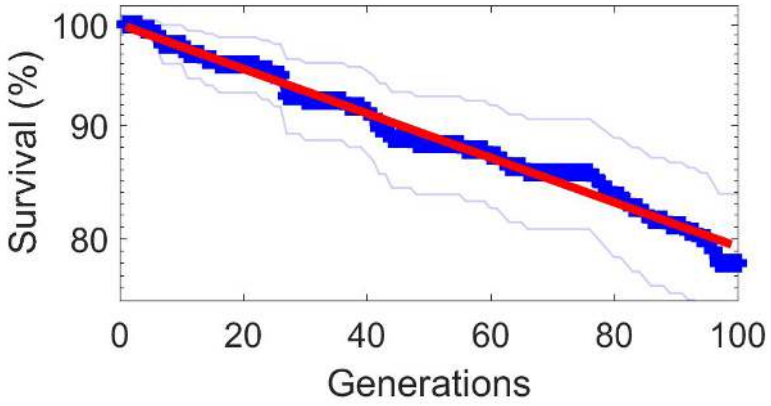

Figure S 11: **Survival of the pMQ strain in a μMA experiment, with or without induction of the mutator allele dnaQ926 by arabinose**

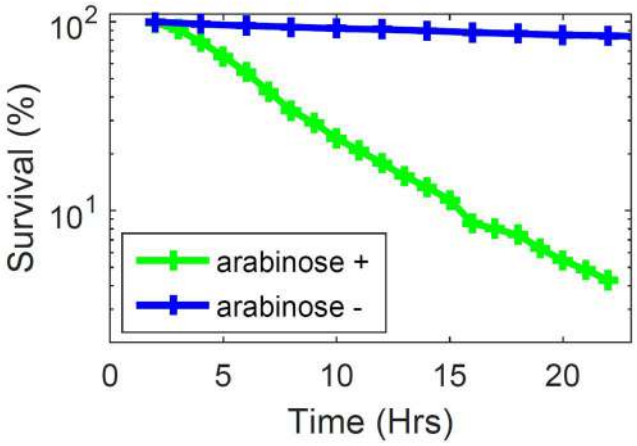

Figure S 12: **Our automatic filtering procedure removes image analysis errors producing aberrantly low or high growth rate values.**
Raw data from the *mutH* μMA experiment shown in figure 3A. Red dots : growth rate values that are detected as aberrant and removed by our procedure; black dots: growth rate values that are kept in our analysis. Importantly, the noise does not affect our estimation of the moments of the DFE, as shown in section 2.3.4. Therefore our filtering procedure improves the visualization of growth rate evolution but does not impact significantly the estimation of DFE moments (see table S5).

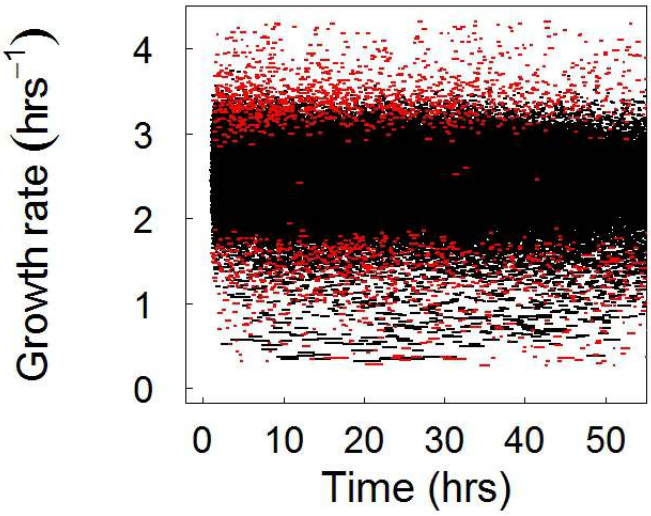

Figure S 13: **Distributions of single-cell growth rate in μMA experiments.** Growth rate distributions (growth rates for all times are pooled) for A) the WT experiment shown in figure 3A (WT n°1) , B) another WT experiment (WT n°2), C) the *mutH* experiment shown in figure 3A. Red curves in A and B are gaussian fits. D) growth rate evolution in WT n°2. The slight assymmetry shown here in panel A creates a slight assymetry in figure 3A, left panel, where we can see a few more data points in high growth rates than in low growth rates. This is due to some slight variations between experiments (we believe it is caused by slight differences in the quality of our images and image analysis) that are not strain-specific, as shown by the other WT experiment represented in panel B and D, which has a more symmetrical distribution

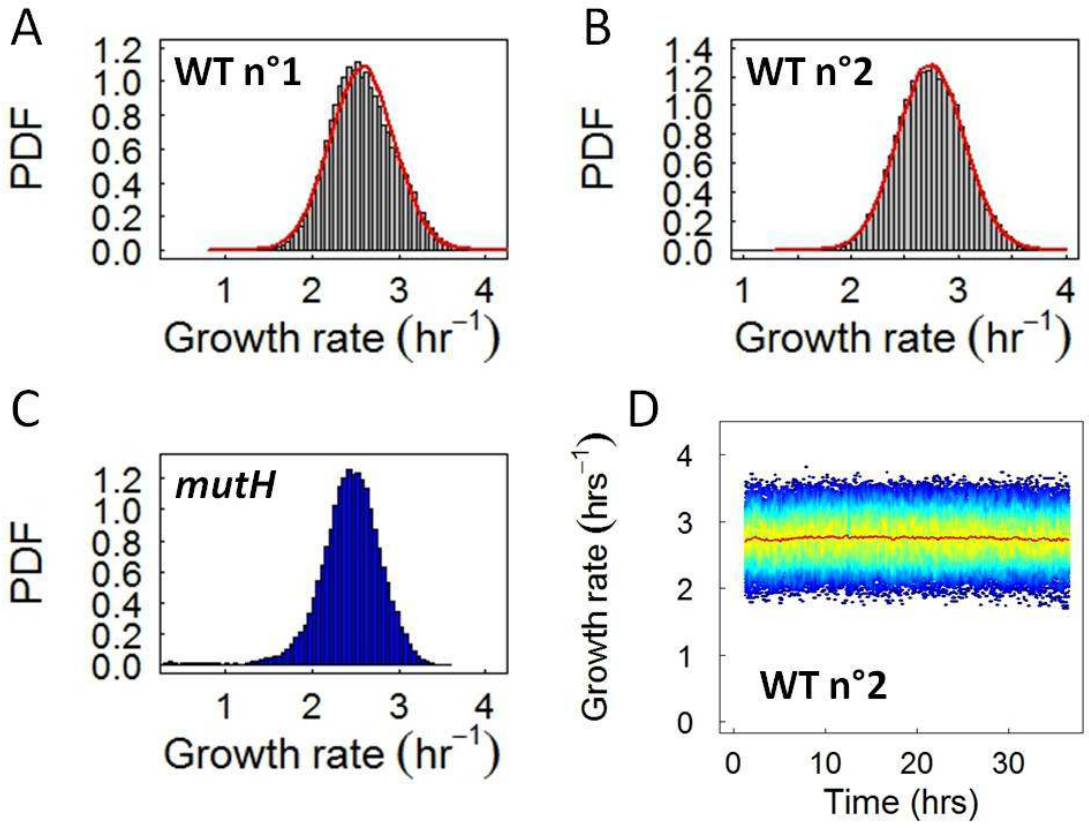

Figure S 14: **Mortality induces noise in the estimation of the DFE's moments.** $E_2(t) = \ln(< W_t^2 >) - 2\ln(< W_t >)$, whose slope is $\lambda < s^2 >$, is plotted for a representative *mutH* μMA experiment, taking all cells (bottom panel, green line) or only the cells that are still alive at 44 hours after the beginning of the experiment (top panel, blue line). R^2 coefficient of determination for linear regressions are indicated in each case (a good fit with a linear regression gives R^2 close to one).

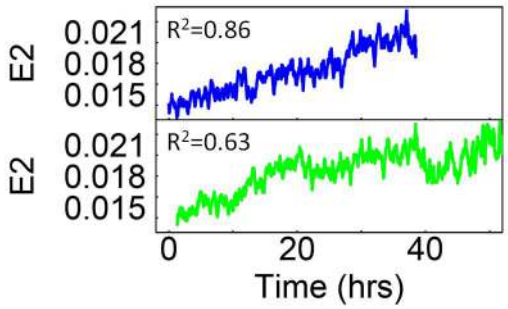

Figure S 15: **The dependency of the replication error rate on growth rate can be explained by the variations in the number of replication forks** The average number of replication forks increases with growth rate. In balanced growth, this translates into a simple relation between these two variables. Nevertheless, here cells that grow slowly are stressed and their cell size is often larger than expected for their rate of growth. This adds some complexity to the expected relation between the average fork number and the growth rate (since the number of forks increases with cell size). Consequently, in order to determine whether the observed dependency of the error rate on growth rate can be explained simply by variations in the number of forks we estimate the number of forks for each single cell in the data, from its size and growth rate. We multiply this estimation by the mean error rate per fork in the cell population (i.e. the average rate of foci occurrence divided by the average estimated number of forks) to get an estimation of the error rate in each single cell. Here black dots represent experimental data, binned by growth rate (i.e.rates of foci occurrence are averaged for subpopulations of cells with similar rate of growth) and the red line shows the theoretical estimations on all single-cells, also binned by growth rate.

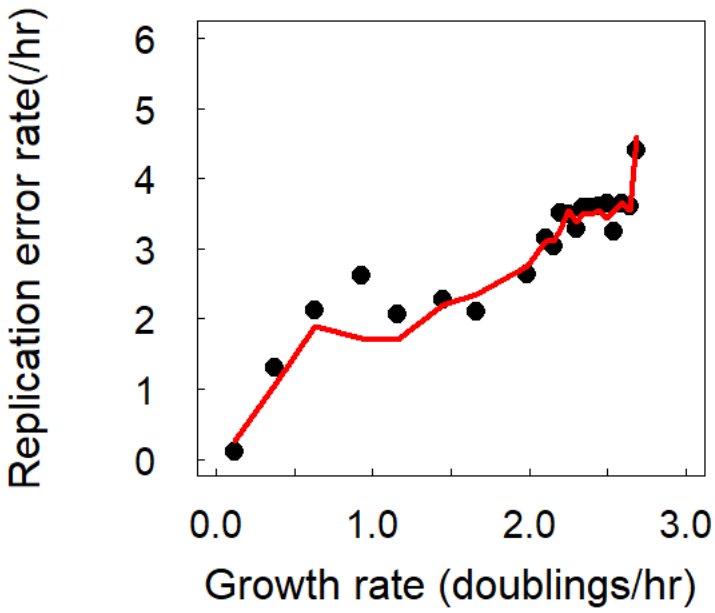

Figure S 16: **Non-parametric estimation of the DFE moments.**
Plot of $E_n(t) = \sum_{k=1}^{n}(-1)^k \binom{n}{k} \ln(\mathbb{E}(W_t^k))$ for n=1,..4, for a representative WT (blue) and *mutH* (cyan) experiment. Red and magenta lines are linear regressions for WT and *mutH* respectively. The WT experiment is a control showing negligible variations of $E_n(t)$. The slope of $E_n(t)$ in *mutH* is the product of the mutation rate and the nth moment of the DFE.

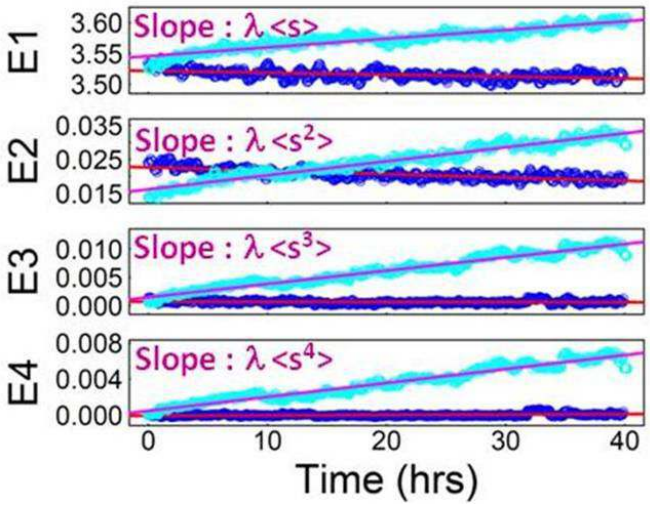

Figure S 17: **Noise in single-cell growth rate .** A) Probability Density Function of single-cell growth rate in WT; B) Autocorrelation function of single cell growth rate in WT as a function of generations; C) Mean and standard deviation of single-cell growth rate are plotted for 50 subpopulations of cells (blue dots), corresponding each to a single microchannel in a *mutH* μMA experiment; we selected 35 microchannels where a strongly deleterious mutation occurred, extracted for each microchannel the growth rates of the mother cells after the mutation occurred and computed the mean and standard deviation; we also randomly selected 15 microchannels where no strongly deleterious mutation occurred and performed the same analysis; the red line is a linear regression

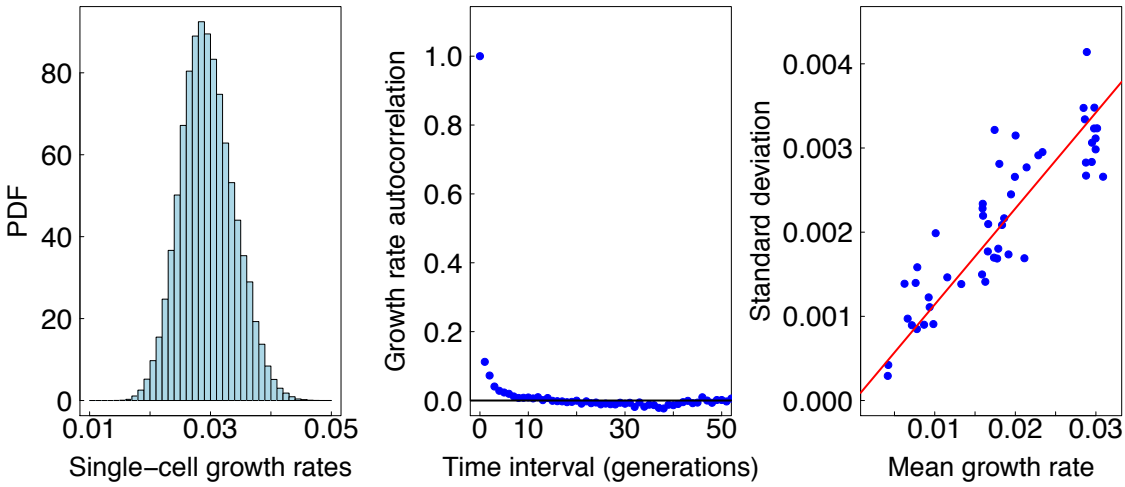

Figure S 18: **μMA simulations are in good agreement with experimental data.** Numerical simulations of μMA experiments, with a constant mutation rate (scenario A section 2.3.5) of 0.32 mutations per hour (identical to our estimation for *mutH* strain) and a Beta distribution with parameters $\alpha = 0.0074$ and $\beta = 2.4$ for the DFE. For each time point, all growth rates are plotted (as in figure 2) and color depicts the local growth rate density (from blue to yellow) and the red line is the evolution of the mean growth rate.

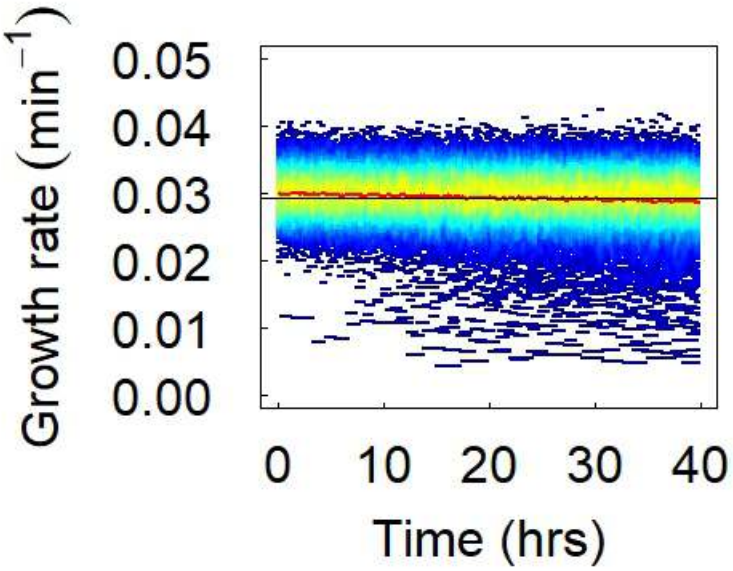

Table S 1: **Mutant frequency measurements in batch cultures**
As explained in section 1.4, we measured the frequency of antibiotic resistant mutants arising during growth of bacterial population in batch cultures. We used either rifampicin or streptomycin and cultured the cells either in LB or Minimal Medium supplemented with arabinose (to induce expression of dnaQ926 in MF1). The Mean and Standard Error of the Mean of mutant frequencies are given

Strain	**Antibiotics**	**Growth medium**	**Mean mutant frequency**	**SEM mutant frequency**
mutH	Streptomycin	LB	$9.4\ 10^{-8}$	$1.6\ 10^{-8}$
mutT	Streptomycin	LB	$1.1\ 10^{-7}$	$0.27\ 10^{-7}$
mutH	Rifampicin	MM arabinose	$1.0\ 10^{-6}$	$0.8\ 10^{-6}$
MF1	Rifampicin	MM arabinose	$1.8\ 10^{-5}$	$3.7\ 10^{-6}$

Table S 2: **Mutation rate, death rate and growth rate decrease in μMA for *mutH*, *mutT* and MF1.** WT dies from aging [13], independently of mutations. Therefore we calculate the mutation-related death rate of each strain by subtracting the death rate of the WT to the death rate of the other strains. The mutation rate is calculated with MutL foci method for WT and *mutH* and from classical genetic assays (see section 1.4) for *mutT* and MF1

	mutH	*mutT*	**MF1**	**WT**
Decrease of average growth rate $(\%/hr)$	0.1	0.07	2.3	< 0.01
Death rate (per hour)	0.004	0.004	0.06	0
mutation rate (per hour)	0.32	0.37	5.6	0.0022

Table S 3: **Estimated slopes of $E_1(t)$, $E_2(t)$, ... $E_{10}(t)$ for all μMA experiments with WT, *mutH* and *mutT* strains.** The moments of the DFE $< s >$,$< s^2 >$,... $< s^{10} >$ are estimated from the slopes of $E_1(t)$, $E_2(t)$, ... $E_{10}(t)$. The coefficient λ is the mutation rate. For *mutH* $\lambda = 0.0054\ min^{-1}$, for *mutT* $\lambda = 0.0063\ min^{-1}$, for MF1 $\lambda = 0.1\ min^{-1}$, and for WT $\lambda = 2.7\ 10^{-5}\ min^{-1}$.

	mutH **Exp1**	*mutH* **Exp2**	*mutH* **Exp3**	*mutT*	**MF1**	**WT Exp1**	**WT Exp2**	**WT Exp3**
Slope of E_1: $\lambda < s > (\cdot 10^5)$	1.9	1.6	1.5	1.2	39	-0.3	0.1	0.3
Slope of E_2: $\lambda < s^2 > (\cdot 10^6)$	6.8	5.2	3.0	2.2	166	-1.5	-1.6	-0.1
Slope of E_3: $\lambda < s^3 > (\cdot 10^6)$	3.9	2.7	1.2	1.6	89	-0.1	-0.09	0.03
Slope of E_4: $\lambda < s^4 > (\cdot 10^7)$	25	16	7.3	9.4	560	0.1	-0.2	0.6
Slope of E_5: $\lambda < s^5 > (\cdot 10^7)$	18	11	4.8	5.5	390	-0.01	0.06	0.4
Slope of E_6: $\lambda < s^6 > (\cdot 10^7)$	13	7.5	3.3	3.5	290	-0.05	0.01	0.2
Slope of E_7: $\lambda < s^7 > (\cdot 10^7)$	9.7	5.5	2.3	2.3	220	-0.04	-0.007	0.1
Slope of E_8: $\lambda < s^8 > (\cdot 10^7)$	7.4	4.2	1.6	1.6	180	-0.03	0.002	0.07
Slope of E_9: $\lambda < s^9 > (\cdot 10^7)$	5.6	3.3	1.2	1.1	150	-0.02	0.001	0.05
Slope of E_{10}:$\lambda < s^{10} > (\cdot 10^7)$	4.3	2.7	0.8	0.8	130	-0.02	-0.002	0.03

Table S 4: **Mean, Coefficient of Variation (CV), skewness and kurtosis of the DFE estimated from μMA experiments with *mutH* (3 independent experiments), *mutT* (1 experiment) and MF1 (1 experiment)**

	mutH **Exp1**	*mutH* **Exp2**	*mutH* **Exp3**	*mutT*	**MF1**
Mean (%)	0.35	0.30	0.28	0.22	0.35
CV	10.0	10.3	8.2	9.2	11
Skewness	16.0	16.6	17.3	35	14
Kurtosis	302	329	446	1040	220

Table S 5: **Estimated slopes of $E_1(t)$, $E_2(t)$, $E_3(t)$, $E_4(t)$ for a representative *mutH* μMA experiment, with or without filtering of aberrant growth rate values (with different threshold parameters T for filtering).**

	MutH T=0.15	**MutH** T=0.2	**MutH** T=0.25	**MutH** T=0.3	**MutH** T=0.35	**MutH** T=0.4	**MutH** T=0.45	**MutH** No filter
Slope of E_1 ($.10^5$)	2.0	1.9	1.9	1.9	2.0	2.0	2.0	1.9
Slope of E_2 ($.10^6$)	6.8	6.5	6.7	6.9	7.1	7.2	7.2	7.8
Slope of E_3 ($.10^6$)	3.9	3.7	3.7	3.9	4.0	4.0	4.0	4.2
Slope of E_4 ($.10^7$)	26	24	24	25	26	26	26	29

Table S 6: **Estimated slopes of $E_1(t)$, $E_2(t)$, $E_3(t)$, $E_4(t)$ for a representative WT μMA experiment, with or without filtering of aberrant growth rate values (with different threshold parameters T for filtering).**

	WT T=0.15	**WT** T=0.2	**WT** T=0.25	**WT** T=0.3	**WT** T=0.35	**WT** T=0.4	**WT** T=0.45	**WT** No filter
Slope of E_1 ($.10^5$)	0.1	0.2	0.1	0.1	0.1	0.1	0.1	0.2
Slope of E_2 ($.10^6$)	-0.9	-1.3	-1.5	-1.6	-1.7	-1.9	-1.9	-1.6
Slope of E_3 ($.10^6$)	-0.005	-0.05	-0.08	-0.09	-0.1	-0.09	-0.1	-0.1
Slope of E_4 ($.10^7$)	-0.2	-0.1	-0.1	-0.2	-0.2	-0.2	-0.3	-1.2

Table S 7: **The 4 first moments of *mutH* DFE estimated from the whole data (including cells that die before the end of the experiment).** As in Figure 3C, mean +/− 2 Standard Error of the Mean for the 3 *mutH* experiments are shown.

	Experimental DFE
Mean	0.0032 +/− 0.0004
Coefficient of Variation	7 +/− 2.3
Skewness	17 +/− 1
Kurtosis	500 +/− 200

Table S 8: **Estimated slopes of $E_1(t)$, $E_2(t)$, $E_3(t)$, $E_4(t)$ for one representative *mutH* μMA experiment with visual detection of cell death or with our automatic procedure to eliminate mortality effects.** λ is the mutation rate of the *mutH* strain : $\lambda = 0.0054\ min^{-1}$

	Visual detection	**Automatic Procedure**
Slope of E_1 : $\lambda < s > (.10^5)$	1.97	1.92
Slope of E_2 : $\lambda < s^2 > (.10^6)$	6.69	6.79
Slope of E_3 : $\lambda < s^3 > (.10^6)$	3.77	3.85
Slope of E_4 : $\lambda < s^4 > (.10^7)$	25.0	25.3

Table S 9: **Bacterial strains and plasmids**

Strain/plasmid	**Genotype**	**Source**
MG1655		E. coli GSC
ME63-01	MG1655, but mutH::cam	This study
ME63-02	MG1655, but mutT::kan	This study
ME63-03	MG1655, but pMQ	This study
63ME120R	MG1655, but *lacZ::yfp-mutL*-frt, *mutL*::frt, *attTn7*::pRNA1-*tdCherry*	This study
63ME121R	63ME120R, but *mutH::cam*	This study
63ME122R	63ME121R, but *mutS::spec/strep*	This study
63ME123R	63ME120R, but *uvrD::phleo*	This study
63ME124R	63ME121R, but *rnhB::kan*	This study
63ME125R	63ME120R, but *mutT::kan*	This study
MF1	MG1655 *att*P21::*araC*-PBad-*dnaQ926*	This study
pMQ		[21]
pNDL32		Paulsson lab

Table S 10: **Estimated DFE moments for simulations of μMA experiments, with *mutH* mutation rate, for scenario A (constant mutation rate) and scenario B (growth rate-dependent mutation rate).** The mutation rate was the one estimated for our *mutH* strain. Mean +/- 2 Standard Error of the Mean ($\frac{\sigma}{\sqrt{(n)}}$) for 30 simulations are shown

	Scenario A	**Scenario B**
1st moment (mean) $.10^3$	3.1 +/- 0.1	3.1 +/- 0.1
2nd moment $.10^4$	9.4 +/- 0.5	8.9 +/- 0.5
3rd moment $.10^4$	4.4 +/- 0.4	3.9 +/- 0.3
4th moment $.10^4$	2.5 +/- 0.3	2.1 +/- 0.2

Table S 11: **Estimated DFE moments for simulations of μMA experiments, with MF1 (dnaQ926) mutation rate (20x higher than *mutH*), for scenario A (constant mutation rate) and scenario B (growth rate-dependent mutation rate).** Mean +/- 2 Standard Error of the Mean ($\frac{\sigma}{\sqrt{(n)}}$) for 30 simulations are shown

	Scenario A	**Scenario B**
1st moment (mean) $.10^3$	3.1 +/- 0.03	2.0+/- 0.02
2nd moment $.10^4$	9.4 +/- 0.1	3.5 +/- 0.07
3rd moment $.10^4$	4.3+/- 0.1	1.1 +/- 0.04
4th moment $.10^4$	2.4 +/- 0.08	0.5+/- 0.03

Table S 12: **Estimated DFE moments for simulations of μMA experiments, with MF1 (dnaQ926) mutation rate (20x higher than *mutH*), for scenario A (constant mutation rate) and scenario B (growth rate-dependent mutation rate).**The moments were estimated only on the begining of the experiment (the first 10 hours). Mean +/- 2 Standard Error of the Mean ($\frac{\sigma}{\sqrt{(n)}}$) for 20 simulations are shown

	Scenario A	**Scenario B**
1st moment (mean) $.10^3$	3.1 +/- 0.05	2.8 +/- 0.06
2nd moment $.10^4$	9.0 +/- 0.3	7.3 +/- 0.3
3rd moment $.10^4$	4.0 +/- 0.2	3.0 +/- 0.2
4th moment $.10^4$	2.2 +/- 0.2	1.5 +/- 0.2

Movie S1. μMA experiment with *mutH* strain (3 days of growth).

Movie S2. MV experiment with *mutH* strain. Top panel : Red fluorescence (constitutive expression of tdCherry). Bottom panel: Yellow fluorescence (YFP-MutL tags replication errors).

References and Notes

1. J. W. Drake, Too many mutants with multiple mutations. *Crit. Rev. Biochem. Mol. Biol.* **42**, 247–258 (2007). doi:10.1080/10409230701495631 Medline

2. S. Uphoff, N. D. Lord, B. Okumus, L. Potvin-Trottier, D. J. Sherratt, J. Paulsson, Stochastic activation of a DNA damage response causes cell-to-cell mutation rate variation. *Science* **351**, 1094–1097 (2016). doi:10.1126/science.aac9786 Medline

3. J. Wang, K. D. Gonzalez, W. A. Scaringe, K. Tsai, N. Liu, D. Gu, W. Li, K. A. Hill, S. S. Sommer, Evidence for mutation showers. *Proc. Natl. Acad. Sci. U.S.A.* **104**, 8403–8408 (2007). doi:10.1073/pnas.0610902104 Medline

4. M. R. Stratton, P. J. Campbell, P. A. Futreal, The cancer genome. *Nature* **458**, 719–724 (2009). doi:10.1038/nature07943 Medline

5. T. Bataillon, S. F. Bailey, Effects of new mutations on fitness: Insights from models and data. *Ann. N.Y. Acad. Sci.* **1320**, 76–92 (2014). doi:10.1111/nyas.12460 Medline

6. T. Mukai, The genetic structure of natural populations of *Drosophila melanogaster*. I. Spontaneous mutation rate of polygenes controlling viability. *Genetics* **50**, 1–19 (1964). Medline

7. T. T. Kibota, M. Lynch, Estimate of the genomic mutation rate deleterious to overall fitness in *E. coli*. *Nature* **381**, 694–696 (1996). doi:10.1038/381694a0 Medline

8. P. D. Keightley, A. Caballero, Genomic mutation rates for lifetime reproductive output and lifespan in *Caenorhabditis elegans*. *Proc. Natl. Acad. Sci. U.S.A.* **94**, 3823–3827 (1997). doi:10.1073/pnas.94.8.3823 Medline

9. A. Eyre-Walker, P. D. Keightley, The distribution of fitness effects of new mutations. *Nat. Rev. Genet.* **8**, 610–618 (2007). doi:10.1038/nrg2146 Medline

10. D. L. Halligan, P. D. Keightley, Spontaneous mutation accumulation studies in evolutionary genetics. *Annu. Rev. Ecol. Evol. Syst.* **40**, 151–172 (2009). doi:10.1146/annurev.ecolsys.39.110707.173437

11. H. Lee, E. Popodi, H. Tang, P. L. Foster, Rate and molecular spectrum of spontaneous mutations in the bacterium *Escherichia coli* as determined by whole-genome sequencing. *Proc. Natl. Acad. Sci. U.S.A.* **109**, E2774–E2783 (2012). doi:10.1073/pnas.1210309109 Medline

12. P. L. Foster, H. Lee, E. Popodi, J. P. Townes, H. Tang, Determinants of spontaneous mutation in the bacterium *Escherichia coli* as revealed by whole-genome sequencing. *Proc. Natl. Acad. Sci. U.S.A.* **112**, E5990–E5999 (2015). doi:10.1073/pnas.1512136112 Medline

13. P. Wang, L. Robert, J. Pelletier, W. L. Dang, F. Taddei, A. Wright, S. Jun, Robust growth of *Escherichia coli*. *Curr. Biol.* **20**, 1099–1103 (2010). doi:10.1016/j.cub.2010.04.045 Medline

14. Materials and methods and supplementary text are available as supplementary materials.

15. M. Elez, A. W. Murray, L.-J. Bi, X.-E. Zhang, I. Matic, M. Radman, Seeing mutations in living cells. *Curr. Biol.* **20**, 1432–1437 (2010). doi:10.1016/j.cub.2010.06.071 Medline

16. R. S. Galhardo, P. J. Hastings, S. M. Rosenberg, Mutation as a stress response and the regulation of evolvability. *Crit. Rev. Biochem. Mol. Biol.* **42**, 399–435 (2007). doi:10.1080/10409230701648502 Medline

17. P. L. Foster, Stress-induced mutagenesis in bacteria. *Crit. Rev. Biochem. Mol. Biol.* **42**, 373–397 (2007). doi:10.1080/10409230701648494 Medline

18. R. Maharjan, T. Ferenci, Mutational signatures indicative of environmental stress in bacteria. *Mol. Biol. Evol.* **32**, 380–391 (2015). doi:10.1093/molbev/msu306 Medline

19. S. Trindade, L. Perfeito, I. Gordo, Rate and effects of spontaneous mutations that affect fitness in mutator *Escherichia coli*. *Philos. Trans. R. Soc. London Ser. B* **365**, 1177–1186 (2010). doi:10.1098/rstb.2009.0287 Medline

20. L. Perfeito, A. Sousa, T. Bataillon, I. Gordo, Rates of fitness decline and rebound suggest pervasive epistasis. *Evolution* **68**, 150–162 (2014). doi:10.1111/evo.12234 Medline

21. K. M. Esvelt, J. C. Carlson, D. R. Liu, A system for the continuous directed evolution of biomolecules. *Nature* **472**, 499–503 (2011). doi:10.1038/nature09929 Medline

22. S. Maisnier-Patin, J. R. Roth, A. Fredriksson, T. Nyström, O. G. Berg, D. I. Andersson, Genomic buffering mitigates the effects of deleterious mutations in bacteria. *Nat. Genet.* **37**, 1376–1379 (2005). doi:10.1038/ng1676 Medline

23. T. A. Sangster, S. Lindquist, C. Queitsch, Under cover: Causes, effects and implications of Hsp90-mediated genetic capacitance. *Bioessays* **26**, 348–362 (2004). doi:10.1002/bies.20020 Medline

24. R. D. Kouyos, O. K. Silander, S. Bonhoeffer, Epistasis between deleterious mutations and the evolution of recombination. *Trends Ecol. Evol.* **22**, 308–315 (2007). doi:10.1016/j.tree.2007.02.014 Medline

25. C. A. Schneider, W. S. Rasband, K. W. Eliceiri, NIH Image to ImageJ: 25 years of image analysis. *Nat. Methods* **9**, 671–675 (2012). doi:10.1038/nmeth.2089 Medline

26. J. Schindelin, I. Arganda-Carreras, E. Frise, V. Kaynig, M. Longair, T. Pietzsch, S. Preibisch, C. Rueden, S. Saalfeld, B. Schmid, J.-Y. Tinevez, D. J. White, V. Hartenstein, K. Eliceiri, P. Tomancak, A. Cardona, Fiji: An open-source platform for biological-image analysis. *Nat. Methods* **9**, 676–682 (2012). doi:10.1038/nmeth.2019 Medline

27. K. Jaqaman, D. Loerke, M. Mettlen, H. Kuwata, S. Grinstein, S. L. Schmid, G. Danuser, Robust single-particle tracking in live-cell time-lapse sequences. *Nat. Methods* **5**, 695–702 (2008). doi:10.1038/nmeth.1237 Medline

28. G. Lehmann, Kappa Sigma clipping. *Insight J.* http://hdl.handle.net/1926/367 (2006).

29. N. Otsu, A threshold selection method from grey-level histograms. *IEEE Trans. Syst. Man Cybern.* **9**, 62–66 (1979). doi:10.1109/TSMC.1979.4310076

30. J. Y. Tinevez, N. Perry, J. Schindelin, G. M. Hoopes, G. D. Reynolds, E. Laplantine, S. Y. Bednarek, S. L. Shorte, K. W. Eliceiri, TrackMate: An open and extensible platform for single-particle tracking. *Methods* **115**, 80–90 (2017). doi:10.1016/j.ymeth.2016.09.016 Medline

31. R. Peto, M. C. Pike, P. Armitage, N. E. Breslow, D. R. Cox, S. V. Howard, N. Mantel, K. McPherson, J. Peto, P. G. Smith, Design and analysis of randomized clinical trials requiring prolonged observation of each patient. II. Analysis and examples. *Br. J. Cancer* **35**, 1–39 (1977). doi:10.1038/bjc.1977.1 Medline

32. M. Elez, M. Radman, I. Matic, Stoichiometry of MutS and MutL at unrepaired mismatches *in vivo* suggests a mechanism of repair. *Nucleic Acids Res.* **40**, 3929–3938 (2012). doi:10.1093/nar/gkr1298 Medline

33. K. A. Datsenko, B. L. Wanner, One-step inactivation of chromosomal genes in *Escherichia coli* K-12 using PCR products. *Proc. Natl. Acad. Sci. U.S.A.* **97**, 6640–6645 (2000). doi:10.1073/pnas.120163297 Medline

34. F. St.-Pierre, L. Cui, D. G. Priest, D. Endy, I. B. Dodd, K. E. Shearwin, One-step cloning and chromosomal integration of DNA. *ACS Synth. Biol.* **2**, 537–541 (2013). doi:10.1021/sb400021j Medline

35. P. Armitage, *Statistical Methods in Medical Research* (Wiley, 2001).

36. A. Zaritsky, P. Wang, N. O. Vischer, Instructive simulation of the bacterial cell division cycle. *Microbiology* **157**, 1876–1885 (2011). doi:10.1099/mic.0.049403-0 Medline

37. M. Radman, R. Wagner, Mismatch repair in *Escherichia coli*. *Annu. Rev. Genet.* **20**, 523–538 (1986). doi:10.1146/annurev.ge.20.120186.002515 Medline

38. N. Y. Yao, J. W. Schroeder, O. Yurieva, L. A. Simmons, M. E. O'Donnell, Cost of rNTP/dNTP pool imbalance at the replication fork. *Proc. Natl. Acad. Sci. U.S.A.* **110**, 12942–12947 (2013). doi:10.1073/pnas.1309506110 Medline

39. T. A. Kunkel, D. A. Erie, Eukaryotic mismatch repair in relation to DNA replication. *Annu. Rev. Genet.* **49**, 291–313 (2015). doi:10.1146/annurev-genet-112414-054722 Medline

40. R. M. Schaaper, B. I. Bond, R. G. Fowler, A•T→C•G transversions and their prevention by the *Escherichia coli mutT* and *mutHLS* pathways. *Mol. Gen. Genet.* **219**, 256–262 (1989). doi:10.1007/BF00261185 Medline

41. A. Gutierrez, L. Laureti, S. Crussard, H. Abida, A. Rodríguez-Rojas, J. Blázquez, Z. Baharoglu, D. Mazel, F. Darfeuille, J. Vogel, I. Matic, β-Lactam antibiotics promote bacterial mutagenesis via an RpoS-mediated reduction in replication fidelity. *Nat. Commun.* **4**, 1610 (2013). doi:10.1038/ncomms2607 Medline

42. H. C. Tsui, G. Feng, M. E. Winkler, Negative regulation of *mutS* and *mutH* repair gene expression by the Hfq and RpoS global regulators of *Escherichia coli* K-12. *J. Bacteriol.* **179**, 7476–7487 (1997). doi:10.1128/jb.179.23.7476-7487.1997 Medline

43. R. S. Harris, G. Feng, K. J. Ross, R. Sidhu, C. Thulin, S. Longerich, S. K. Szigety, M. E. Winkler, S. M. Rosenberg, Mismatch repair protein MutL becomes limiting during stationary-phase mutation. *Genes Dev.* **11**, 2426–2437 (1997). doi:10.1101/gad.11.18.2426 Medline

44. R. M. Schaaper, M. Radman, The extreme mutator effect of *Escherichia coli mutD5* results from saturation of mismatch repair by excessive DNA replication errors. *EMBO J.* **8**, 3511–3516 (1989). Medline

45. P. Y. Ho, A. Amir, Simultaneous regulation of cell size and chromosome replication in bacteria. *Front. Microbiol.* **6**, 662 (2015). doi:10.3389/fmicb.2015.00662 Medline

46. S. Taheri-Araghi, S. Bradde, J. T. Sauls, N. S. Hill, P. A. Levin, J. Paulsson, M. Vergassola, S. Jun, Cell-size control and homeostasis in bacteria. *Curr. Biol.* **25**, 385–391 (2015). doi:10.1016/j.cub.2014.12.009 Medline